Aalto University School of Electrical Engineering

Magnetic resonance imaging -based radiation therapy

Methods enabling the radiation therapy treatment planning workflow for prostate cancer patients by relying solely on MRI-based images throughout the process

Juha Korhonen

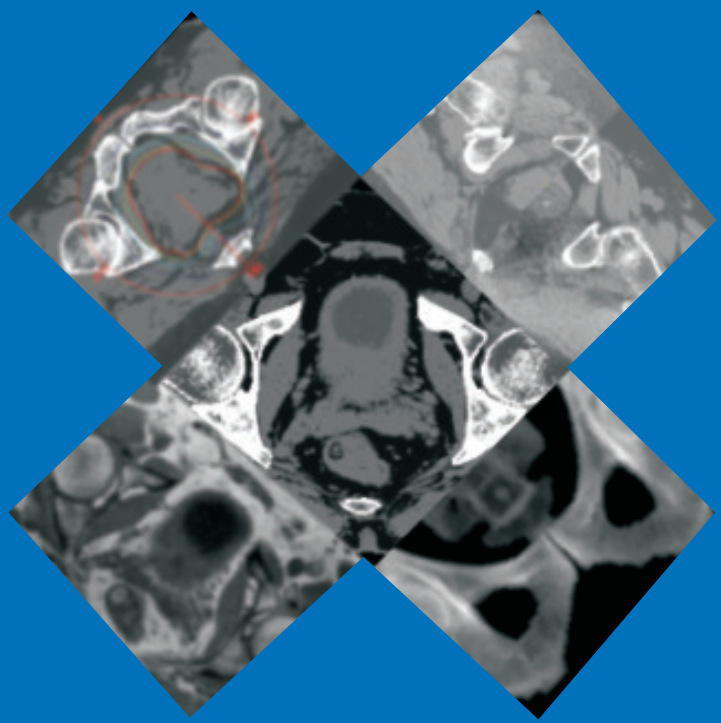

Aalto University

DOCTORAL DISSERTATIONS

Aalto University publication series
DOCTORAL DISSERTATIONS 35/2015

Magnetic resonance imaging -based radiation therapy

Methods enabling the radiation therapy treatment planning workflow for prostate cancer patients by relying solely on MRI-based images throughout the process

Juha Korhonen

A doctoral dissertation completed for the degree of Doctor of Science (Technology) to be defended, with the permission of the Aalto University School of Electrical Engineering, at a public examination held at the lecture hall S1 of the school on 30 April 2015 at 12.

Aalto University
School of Electrical Engineering
Department of Electrical Engineering and Automation
Health Technology

Supervising professor
Professor Raimo Sepponen

Thesis advisors
Docent Mika Kapanen, HUCH Cancer Center, Helsinki University Central Hospital, Finland
Docent Mikko Tenhunen, HUCH Cancer Center, Helsinki University Central Hospital, Finland

Preliminary examiners
PhD Tufve Nyholm, Department of Radiation Sciences, Umeå University, Sweden
PhD Teo Stanescu, Department of Radiation Oncology, University of Toronto, Canada

Opponent
Professor Peter Greer, Department of Radiation Oncology / Physics, University of Newcastle, Australia

Aalto University publication series
DOCTORAL DISSERTATIONS 35/2015

ISBN 978-952-60-6123-8 (printed)
ISBN 978-952-60-6124-5 (pdf)
ISSN-L 1799-4934
ISSN 1799-4934 (printed)
ISSN 1799-4942 (pdf)
http://urn.fi/URN:ISBN:978-952-60-6124-5

Unigrafia Oy
Helsinki 2015

Finland

441 697
Printed matter

Aalto University

Abstract

Aalto University, P.O. Box 11000, FI-00076 Aalto www.aalto.fi

Author
Juha Korhonen

Name of the doctoral dissertation
Magnetic resonance imaging -based radiation therapy

Publisher School of Electrical Engineering

Unit Department of Electrical Engineering and Automation

Series Aalto University publication series DOCTORAL DISSERTATIONS 35/2015

Field of research Health Technology

Manuscript submitted 15 October 2014 **Date of the defence** 30 April 2015

Permission to publish granted (date) 2 January 2015 **Language** English

☐ **Monograph** ☒ **Article dissertation (summary + original articles)**

Abstract

This study introduces a radiation therapy treatment planning (RTP) workflow for prostate cancer patients that relies solely on magnetic resonance imaging (MRI) -based RTP images throughout the process.

Scanner-specific intensity values of T1/T2*-weighted in-phase MR images and Hounsfield units (HUs) of computed tomography (CT) images in the male pelvis were analyzed. The results were utilized to generate a dual model conversion technique transforming the MRI data into pseudo-HUs by separate conversion models within and outside of bone segment. The technique was implemented by constructing pseudo-CT images for 15 prostate cancer patients. The feasibility of the obtained images for RTP was evaluated by comparisons against the standard CTs. Dose distributions were analyzed e.g. with volumetric-modulated arc therapy calculated by means of a Monte Carlo algorithm. The feasibility of MRI-based reference images for image guidance was investigated for patient position verification with X-ray -based localization images. The potential susceptibility-induced bone outline shift in MR images and the effect of different bone parts to the absorbed dose were quantified with a dedicated fresh bone phantom.

The local soft- and bony tissue presentation uncertainties in the pseudo-CTs were on average 11 HUs and 99 HUs, respectively. The prostate dose level differences between those in pseudo-CTs and those in CTs ranged from -1.0% to 0.8%. The percentages of dose points in the body passing the 1 mm & 1% 2D gamma index criteria between the images ranged from 79% to 100%. The maximum dose distribution inconsistency behind the bones was 1.3% measured for a single 6 MV radiation field. The bone outlines in the MR images were illustrated correctly within a 1 mm-pixel size, but each 1 mm-sized systematic error in bone segmentation resulted in ~0.4% change to the prostate dose level in the pseudo-CTs. The SDs of differences between cone-beam CT (CBCT)-to-pseudo and CBCT-to-CT automatic registrations were ≤1.0 mm & ≤0.7°. The SDs of differences between pseudo-digitally reconstructed radiograph (DRR) and CT-DRR -based manual registrations with planar localization were ≤1.0 mm (kV) & ≤1.7 mm (MV).

This work shows that it is possible to construct heterogeneous pseudo-CTs of the pelvis by transforming the intensity values of a single MR image into pseudo-HUs, and that by adopting these images for dose calculation and image guidance, the entire MRI-based RTP workflow for prostate cancer patients can be conducted according to required standards of modern RT.

Keywords MRI-based RT, radiotherapy, treatment planning, magnetic resonance imaging

ISBN (printed) 978-952-60-6123-8 **ISBN (pdf)** 978-952-60-6124-5

ISSN-L 1799-4934 **ISSN (printed)** 1799-4934 **ISSN (pdf)** 1799-4942

Location of publisher Helsinki **Location of printing** Helsinki **Year** 2015

Pages 64 **urn** http://urn.fi/URN:ISBN:978-952-60-6124-5

Tekijä
Juha Korhonen

Väitöskirjan nimi
Magneettikuvaus -pohjainen sädehoito

Julkaisija Sähkötekniikan korkeakoulu

Yksikkö Sähkötekniikan ja automaation laitos

Sarja Aalto University publication series DOCTORAL DISSERTATIONS 35/2015

Tutkimusala Terveysteknologia

Käsikirjoituksen pvm 15.10.2014 **Väitöspäivä** 30.04.2015

Julkaisuluvan myöntämispäivä 02.01.2015 **Kieli** Englanti

☐ **Monografia** ☒ **Yhdistelmäväitöskirja (yhteenveto-osa + erillisartikkelit)**

Tiivistelmä

Tämä työ esittelee magneettikuvaus -pohjaisen sädehoidon suunnitteluketjun eturauhassyöpäpotilaille.

Tietyn magneettikuvauslaitteen T1/T2*-painotettuja kuvia ja tietokonetomografia (TT) -kuvia lantion alueesta vertailtiin keskenään, ja tulosten perusteella kehitettiin konversiotekniikka, joka muuntaa magneettikuvan intensiteettiarvot pseudo-Hounsfield yksiköiksi erikseen luu-segmentin sisä- ja ulkopuolella. Tekniikkaa käytettiin pseudo-TT-kuvien muodostamiseksi 15 eturauhassyöpäpotilaalle. Kuvien soveltuvuus sädehoidon suunnitteluun arvioitiin TT-kuvien kanssa suoritettujen vertailutestien avulla. Annosjakaumia analysoitiin esimerkiksi käyttämällä intensiteettimuokattua kaarihoitoa yhdessä Monte Carlo annoslaskenta-algoritmin kanssa. Kuvien käyttökelpoisuus kuvantaohjauksen referenssi-kuviksi tutkittiin kartiokeila-TT (KKTT) ja tasoröntgenkuva -pohjaisille lokalisointi menetelmille. Potentiaalinen luun reunan paikan kemiallinen siirtymä magneettikuvissa, sekä eri luuosien vaikutus absorboituneeseen säteilyannokseen määritettiin luu-liivate -testikohteen avulla.

Pseudo-TT-kuvissa kudosten paikallinen Hounsfield yksiköiden epävarmuus oli keskimäärin 11 pehmytkudoksissa ja 99 luukudoksissa. Eturauhasen säteilyannostason erot pseudo-TT- ja TT-kuvien välillä olivat -1.0%–0.8%. Lisäksi, 79%–100% annoslaskentapisteistä lantion alueella täyttivät 1 mm & 1% 2D gamma-indeksi -kriteerit kuvien välillä. Suurin ero annosjakaumassa luiden takana yhtä 6 MV säteilykenttää käytettäessä oli 1.3%. Magneettikuvissa luun reunan paikka oli esitetty oikein 1 mm pikselikoon tarkuudella, mutta kukin 1 mm -kokoinen systemaattinen virhe luiden segmentoinnissa aiheutti ~0.4% muutoksen eturauhaseen laskettuun säteilyannostasoon pseudo-TT-kuvissa. Keskipoikkemat automaattisten KKTT-pseudo ja KKTT-TT -kuvarekisteröintien välillä olivat ≤1.0 mm & ≤0.7°. Vastaavat erot tasolokalisointikuvien perusteella (referenssinä pseudo-TT- ja TT-kuvista digitaalisesti rekonstruktuoidut röntgenkuvat) suoritetuissa manuaalisissa rekisteröinneissä olivat ≤1.0 mm (kV) & ≤1.7 mm (MV).

Tämä työ osoittaa, että on mahdollista muodostaa heterogeeninen pseudo-TT-kuva lantion alueesta muuntamalla magneettikuvan intensiteettiarvot pseudo-Hounsfield yksiköiksi, ja että kyseistä kuvaa käyttämällä sädehoidon annoslaskennassa ja kuvantaohjauksessa, kaikki eturauhassyöpäpotilaiden magneettikuvaus -pohjaisen sädehoidon suunnitteluketjun työvaiheet voidaan suorittaa tarkasti nykyaikaisen sädehoidon edellyttämillä menetelmillä.

Avainsanat Sädehoito, sädehoidon suunnittelu, magneettikuvaus, eturauhassyöpä

ISBN (painettu) 978-952-60-6123-8 **ISBN (pdf)** 978-952-60-6124-5

ISSN-L 1799-4934 **ISSN (painettu)** 1799-4934 **ISSN (pdf)** 1799-4942

Julkaisupaikka Helsinki **Painopaikka** Helsinki **Vuosi** 2015

Sivumäärä 64 **urn** http://urn.fi/URN:ISBN:978-952-60-6124-5

Acknowledgements

This project was named after the research contract between Elekta Ltd and the Clinical Research Institute Helsinki University Central Hospital (HUCH) Ltd, and was performed in the HUCH Cancer Center (9/2011-8/2014). I want to thank Elekta, the Clinical Research Institute and the HUCH Cancer Center for inviting me to this interesting and challenging project, and for allowing me to complete my PhD Degree within it. In addition to the publications presented in this work, also 6 conference papers about the work were published and presented at international conferences during the project. I've had also the honor of having been invited to give presentations in clinics, meetings and conferences on 12 occasions.

I am sincerely grateful for the positive attitude and other contributions of a number of amazing people. I owe my deepest gratitude to my supervisors Docent Mika Kapanen and Docent Mikko Tenhunen. Their ideas and inspirations constructed the ground for the project and have been supporting it throughout the process. Although they have needed to primarily focus on their daily duties in the clinic, and although they have been involved in many other projects in addition to this one, their doors have always been open for me to guide me through the project and to offer scientific brainstorming. I want to underline my appreciation of Mikko Tenhunen for his supervision in the field of medical physics and for offering me many exciting employment possibilities with radiation therapy during the first five years of my career. I want to highlight also other contributing authors of the publications presented in this work for their interest and efforts in the project: Thank you Docent Jani Keyriläinen, PhD Tiina Seppälä, MSc Laura Tuomikoski, PhD Eero Salli, and PhD Jan-Jakob Sonke. Especially I wish to thank PhD Leonard Wee for his support and contribution to the project in his post as a research manager of Elekta, and also nowadays when working with other duties elsewhere. I also want to thank Professor Raimo Sepponen for his valuable guidance throughout my university studies.

I had the honour of having PhD Teo Stanescu and PhD Tufve Nyholm as the preliminary examiners of the Thesis. I wish to express my sincerest gratitude to the examiners for their sound and valuable comments. I am also privileged to have Professor Peter Greer as the opponent for the Thesis.

There are so many names I would like to highlight here. As I should try to keep this section at least shorter than the actual Thesis itself, let me just jointly address my appreciation to all my colleaques and others who I have been honoured to meet and

work with during the past couple of years: Thank you. The atmosphere has been awesome!

Last but not least; I wish to express my gratitude to the dearest ones. To have you in my life is prizeless.
…My darling wife; it is amazing how well you spread positive energy in my direction. You can illuminate even the polar nights. Living the life with you is simply wonderful. Among other things, I am grateful that we can discuss anything, and that you have been very supportive towards my work. Your continuous support was essential especially during the periods I was focusing on my work at the expense of our precious time together. Thank you.
…My parents and siblings; there are no words to express my thankfulness for our family, for the time we spend together, and for always being there for me. I am grateful for so many lessons to my parents. I feel privileged to have been raised by you. I am sure that many goals which I have reached in my life could not have been reached without you in my life. Thank you for your continuous support and endless love.
…My closest friends; it is unbelievable how effectively you "recharge my batteries". Consequently, your contribution to my work has been surprisingly enormous, even though I guess some of you have no clue whatsoever about the work I've been conducting…. ☺

Helsinki, 7 February 2015

Juha Korhonen

Contents

List of Abbreviations and Symbols

2D	two-dimensional
3D	three-dimensional
6D	six-dimensional
AAA	anisotropic analytical algorithm
ART	adaptive radiation therapy
CBCT	cone-beam computed tomography
CT	computed tomography
CTV	clinical target volume
DRR	digitally reconstructed radiograph
DVH	dose-volume-histogram
ED	electron density
FGE	fast gradient echo
FSE	fast spin echo
FOV	field-of-view
HU	Hounsfield unit
HUCH	Helsinki University Central Hospital
IC	ionization chamber
IGRT	image-guided radiation therapy
IMRT	intensity-modulated radiation therapy
IS	inferior-superior
MC	Monte Carlo
MR	magnetic resonance
MRI	magnetic resonance imaging
MU	monitor unit

OAR	organ-at-risk
PA	posterior-anterior
PD	proton density
PTV	planning target volume
QA	quality assurance
RF	radiofrequency
RL	right-left
ROI	region-of-interest
RT	radiation therapy
RTP	radiation therapy treatment planning
SD	standard deviation
SE	spin echo
T_1	longitudinal relaxation time
T_2	transverse relaxation time
T_2*	apparent transverse relaxation time
TE	echo time
TR	repetition time
VMAT	volumetric-modulated arc therapy
VOI	volume-of-interest
XVMC	X-ray Voxel Monte Carlo

List of Publications

This doctoral dissertation consists of a summary and of the following publications which are referred to in the text by their numerals.

I **J. Korhonen**, M. Kapanen, J. Keyriläinen, T. Seppälä, L. Tuomikoski, and M. Tenhunen; *"Absorbed doses behind bones with MR image-based dose calculations for radiotherapy treatment planning,"* Med. Phys. 40(011701), 1-10 (2013).

II **J. Korhonen**, M. Kapanen, J. Keyriläinen, T. Seppälä, and M. Tenhunen; *"A dual model HU conversion from MRI intensity values within and outside of bone segment for MRI-based radiotherapy treatment planning of prostate cancer,"* Med. Phys. 41(011704), 1-13 (2014).

III **J. Korhonen**, M. Kapanen, J. Keyriläinen, T. Seppälä, L. Tuomikoski, and M. Tenhunen; *"Influence of MRI-based bone outline definition errors on external radiotherapy dose calculation accuracy in heterogeneous pseudo-CT images of prostate cancer patients;"* Acta Oncol. 53(8), 1100-1106 (2014).

IV **J. Korhonen**, M. Kapanen, J.-J. Sonke, L. Wee, E. Salli, J. Keyriläinen, T. Seppälä, and M. Tenhunen; *"Feasibility of MRI-based reference images for image-guided radiotherapy in the pelvis with either cone-beam computed tomography or planar localization images,"*Acta Oncol. Ahead of print, 1-7 (2014).

Author's Contribution

I: *"Absorbed doses behind bones with MR image-based dose calculations for radiotherapy treatment planning"*

The author participated in planning of the examinations and was responsible for designing and constructing the bone and gelatine phantom and for conducting the phantom imaging. The author conducted the dose measurements, the pseudo-CT construction, the treatment planning, the dose calculation, and the data analysis. The author wrote the paper as the corresponding author.

II: *"A dual model HU conversion from MRI intensity values within and outside of bone segment for MRI-based radiotherapy treatment planning of prostate cancer"*

The author participated in planning of the study. The author conducted the patient selection, the data collection from the images, the generation of the soft tissue conversion model, the enhancement of the bone conversion model, introducing the dual model HU conversion technique, the pseudo-CT construction, the pseudo-CT image quality tests, the treatment planning, the dose calculation, and the data analysis. The author wrote the paper as the corresponding author.

III: *"Influence of MRI-based bone outline definition errors on external radiotherapy dose calculation accuracy in heterogeneous pseudo-CT images of prostate cancer patients"*

The author participated in planning of the investigations. The author was responsible for conducting the bone outline location measurements with the dedicated phantom constructed also for the examinations of the publication I, and conducted the image-based bone outline location measurements, the construction of the pseudo-CTs, the treatment planning, the dose calculation, and the data analysis. The author wrote the paper as the corresponding author.

IV: *"Feasibility of MRI-based reference images for image-guided radiotherapy in the pelvis with either cone-beam computed tomography or planar localization images"*

The author participated in planning of the study. The author conducted the patient selection, the pseudo-CT construction, the DRR reconstruction, the automatic patient position verification, and the data analysis. The author directed the research group conducting the manual patient position verifications. The author wrote the paper as the corresponding author.

1. Introduction

1.1 Radiation therapy treatment planning

Radiation therapy (RT) constitutes one of the three major cancer treatment methods, in addition to surgery and medication. RT is a carefully planned multi-tasked process conducted individually for each patient from the prescription to the radiation delivery according to the required standards of modern RT. This RT treatment planning (RTP) workflow begins with a procedure called RT simulation, which includes patient imaging with a carefully planned positioning that needs to be repeated for the treatment delivery. The obtained RTP images of patient anatomy are employed throughout the workflow; i.e. for target delineation, dose calculation, and image guidance. Target delineation is a process conducted to contour target volumes and healthy organ constraints into the RTP images. The contoured images are then applied to dose calculation part of the process that includes planning of the treatment technique and field directions. Image-guided RT (IGRT) employs RTP images as a reference against localization images to verify patient treatment positioning similar to that in RT simulation. The localization images are applied before the treatment delivery by means of imaging modalities integrated with the RT treatment device, e.g. X-ray -based imaging modalities integrated with a linear accelerator.

The RTP images need to provide information to conduct the RTP workflow. For each task in the process it is important that the images visualize the heterogeneous patient anatomy with high spatial resolution. To enable dose calculation in external RT, it is essential that the images present the patient anatomy including body outline with natural heterogeneity of tissue electron density (ED) information [1, 2]. The image data are applied to the computationally conducted dose calculation with algorithms in RTP systems. These dose calculation engines are configured with the output of the treatment device in use.

1.2 CT-based radiation therapy

Conventionally, the external RTP workflow is conducted by relying on three-dimensional (3D) anatomical information acquired with a computed tomography (CT) scanner. The CT simulator is equipped with such accessories as a flat indexed couch, a laser-localization system and patient immobilization to enable imaging in RT treatment position [1, 2]. The imaging is based on the transmission measurements of narrow X-ray beams rotating 360° around the patient lying on a couch which is

moving through the scanner aperture (helical CT) [1, 2]. The method enables reconstruction of geometrically accurate 3D images presenting the distribution of attenuation coefficients as Hounsfield units (HUs) [1, 2]. The linear relationship between HUs and attenuation coefficients enables voxel-by-voxel calibration of HUs to tissue EDs relative to that of water [1-5]. The scanner-specific HU-to-ED calibration is verified with phantom measurements in regular quality assurance (QA) with respect to accuracy criterion of ~20 HUs enabling dose calculations in the natural heterogeneous presentation of human body EDs [1-10]. Consequently, CT imaging is regarded as the standard for dose calculation in modern RT. CT images can also be adopted as reference for 3D or 6D IGRT techniques achieving patient position corrections through automatic registration between the RTP images and cone-beam CT (CBCT) localization images [11-13]. The bony tissue presentative digitally reconstructed radiographs (DRRs) can be reconstructed from CT to obtain reference images also for the IGRT methods relying on 2D planar localization [1, 2].

1.3 MRI in radiation therapy

The soft tissue contrast in CT images is inferior to the soft tissue visibility in magnetic resonance (MR) images, and thus MR images are increasingly employed for RT target delineation [14-16]. As a multi-parametric imaging modality, MRI can provide a powerful integration of anatomical details including also other clinically relevant information e.g. tissue metabolism and functionality [16-19]. A basic difference with MRI compared to CT is that the imaging is performed without ionizing radiation. MRI relies on natural magnetic properties of protons in Hydrogen nuclei [17, 18]. Imaging is accomplished at the presence of a strong static magnetic field adjusting the net magnetization of the protons to the direction of the magnetic field. The aligned magnetization of protons can be excited by applying radiofrequency (RF) pulses. The excited protons emit an MR signal, which can be measured with a receiver RF coil. The spatial location of the MR signal is obtained by varying the main magnetic field with magnetic field gradients. The localization is based on the relationship between magnetic field strength, and precession frequency and phase of the nuclei. The MR signal is highly dependent of a complex combination of tissue properties and chemical environment of Hydrogen. Consequently, the relation between MR signals and EDs is inexplicit. This section presents the challenges faced if aiming to introduce MRI-based RT in a clinic, and introduces previous research conducted for MRI-based RT, focusing on the pelvis.

MRI-based RT: challenges and motivation

The magnetic field and the MR signal measurement cause special requirements for the accessories needed to enable imaging by following the general requirements of RT patient positioning. To employ MR scanner as the primary or only image source for RTP, i.e. to construct an MR simulator for MRI-based RT, the scanner should be equipped with such accessories as MR-compatible patient immobilization, flat table top, laser-localization system and MR signal receiver coil frame [20, 21]. Without

these accessories the patient positioning in imaging would generally not be the same as in RT treatment situation.

The inherent geometrical distortion in MR images and the lack of explicit relation between MR signals and EDs are the major restrictive factors for use of MR images throughout the RTP workflow. Consequently, the increasingly applied RTP workflow necessitates patient imaging with two modalities: MRI for target delineation and CT for dose calculation and image guidance. Although this workflow is built on the main benefits of these imaging modalities for RT, the process also has its downsides: it 1) increases RTP uncertainty by requisite image co-registration, 2) is resource-intensive, 3) is time-consuming, and 4) exposes patients' healthy tissues to the additional ionizing radiation applied in CT. These drawbacks could be avoided by solely resorting to MR images throughout the RTP process, and thus have motivated research introducing methods enabling MRI-based RT. MRI-based dose calculation could enable also on-line adaptive RT (ART) treatment in dedicated MRI-guided RT treatment facilities, or with such new technological developments for IGRT as MR scanners integrated with either a linear accelerator (MRI-Linac) or a Cobalt-60 radiation source (MRI-^{60}Co system, ViewRay®, Oakwood Village, OH, USA) [22-31]. With these MRI-guided RT techniques, it would be particularly reasonable to rely solely on MR images throughout the RTP process.

Influence of geometrical distortion on RTP accuracy

The inherent geometrical distortion in MR images can limit the possibilities for accurate MRI-based RT or even prevent the adoption of some MR platforms into the RT process. In addition to the potential influence of geometric errors on target delineation and image guidance, geometrical distortion could also influence the dose calculation accuracy in the MRI-based RTP workflow. As an example: for a single 6 MV beam, >1 cm error in patient body contour can introduce >3% dose calculation errors, thus not achieving international recommendations on dose calculation accuracy and not leaving room for other error possibilities to reach sufficient overall accuracy level of modern RT [1, 2, 32-34]. The ultimate dose calculation accuracy goal of 1% could potentially be reached with multi-field treatment plans if the average body contour shift is within few millimetres [1, 2, 32-34]. Sub-mm-sized geometric errors introduce no considerable uncertainties for dose calculation or IGRT, and thus do not limit the possibilities for accurate MRI-based RT.

The geometric accuracy depends on the scanner type, distance from the scanner isocenter and quality of geometric correction software, and thus the distortion magnitudes can range from sub-mms up to >2 cm [20, 21, 35-50]. Consequently, the geometric accuracy needs to be carefully evaluated in the commissioning of each MR simulator. Recent studies have shown that the geometric errors can be within acceptable limits for RTP, and thus several research groups have concluded that the geometrical distortion is no restrictive issue for MRI-based RTP in the head or in the pelvis [20, 35-45].

Previous studies have mainly focused on evaluating the system-related distortion caused by magnetic field inhomogeneities and imaging gradient nonlinearities by conducting examinations with synthetic phantom materials. The magnetic susceptibility variations between different body tissues and chemical shift effects can result in additional geometric errors by shifting and distorting the tissue boundaries in the patient MR images [17, 18, 20, 21, 37, 50-54]. Susceptibility differences create small local magnetic field gradients and may cause low MR image intensities for the tissue boundary in images obtained with gradient echo (GE) sequences due to spin dephasing within a voxel. Local magnetic field variations generated by the susceptibility effect are also added to the image encoding gradients, and the shift of a voxel position coordinate may be either positive or negative depending on the direction of the encoding gradient, and the shape and the orientation of the volumes having different susceptibilities [17, 18].

In addition to quantifying the system-related distortion, Kapanen et al. evaluated magnitudes also for the patient-induced distortions including gradient non-linearity, magnetic field distortions and susceptibility differences between the soft tissues and the air with the MR simulator 1.5 T imager GE Optima MR450w (GE Medical Systems Inc., Waukesha, WI, USA) [20]. The geometric errors measured in the ADNI geometric phantom within ± 9 cm from the magnet isocenter were on average within 0.3 mm with the maximum deviation of 0.7 mm [20]. The determined location errors for the body outline contour of the pelvis and for the interface between soft tissue and rectal gas were on average ~1 mm with maximum errors of 5 mm and 2 mm, respectively [20]. This accuracy can be considered sufficient for MRI-based RT in the pelvis because sub-mm-sized errors in internal anatomy cannot result in substantial target delineation or patient positioning failures, and body contour shifts of few millimetres would not introduce >1% dose calculation uncertainty. However, the study did not quantify the potential bone outline shift stemming from substantially different susceptibility values of bone cortex and surrounding soft tissues [20, 50-56].

Representing HUs by pseudo-CT images

The human tissues include genuine variety of EDs [56-58]. In the pelvis, the EDs range from those in high density bony tissues to those in low density soft tissues (EDs from ~1.90 to ~0.90, i.e. from ~1500 HU to ~-100 HU) [1-5, 56-58]. In MRI-based RT, the ED information is represented by reconstructing so-called pseudo-CT images, which include at least a simplified representation of the body tissues as pseudo-HUs [35-38, 59-70].

With conventional techniques suggested for the pelvis, the pseudo-CTs are constructed by assigning the entire body as water-equivalent, or additionally by setting a separate single pseudo-HU for a whole bone segment to separately represent the low density soft tissues and the high density bony tissues [35-37, 60-62]. Eilertsen et al. contoured only the most dense pelvic bone parts and assigned this segment with a pseudo-HU higher than that of water [59]. However, with these methods the heterogeneous human tissue ED information is represented only by one or two

assigned pseudo-HUs leading to considerable simplification of patient anatomy. The HU misrepresentation is substantial especially within the bone segment, in which the natural EDs range from those in the high density bone cortex to those in low density core (the cortical bone: ED ~1.90 i.e. ~1500 HU, and the fatty bone marrow: ED ~0.98 i.e. ~-20 HU, respectively) [1-5, 56-58].

Kapanen & Tenhunen suggested that heterogeneous bony tissue representation could be achieved by converting the intensity values of T_1/T_2*-weighted MR image (obtained by the 1.5 T imager GE Optima MR450w) into pseudo-HUs within the contoured bones and representing only the body volume outside of the bone segment with a homogeneous value [64]. The major benefits of this method include its possibility to obtain pseudo-HUs for the bones from data of a single MR image achieved by a clinically available MRI sequence, and allowing an increase in heterogeneity of tissue representation in pseudo-CTs compared to manual assignment of bulk pseudo-HU to the entire bone segment. Nevertheless, the study did not evaluate explicitly HU accuracy for different bony tissues in the obtained pseudo-CTs, and did not provide a solution for obtaining information about heterogeneous soft tissue HUs. Soft tissues, especially muscle and fat, comprise a large proportion of body volume in the pelvis, and their relative amounts can vary considerably between individuals. If representing these tissues, in which relative EDs to water vary roughly between 0.90 (~-100 HU) and 1.05 (~50 HU), as a homogeneous segment, it is likely that the average soft tissue ED is misrepresented for individual patient anatomies [1-5, 56-58]. Inclusion of soft tissues into pseudo-CTs could potentially improve the MRI-based dose calculation accuracy and enable IGRT with the state-of-the-art method relying on the current position of the moving organs.

Johansson et al. proposed a technique applying MRI data to generate heterogeneous pseudo-CTs of the head [67-69]. The method employs voxel value combinations of three MR image series, out of which two image series were achieved with dual echo ultra-short echo time (TE) sequences and one with T_2-weighted 3D spin echo (SE) sequence. The technique is greatly potential to obtain heterogeneous pseudo-CTs of various body parts because it enables also separation of the bone cortex and the air cavities without a need of segmentation. MRI sequences with extremely short TEs are currently clinically unavailable that can delay wide adoption of the technique.

Dowling et al. proposed that ED information for prostate cancer patients could be adopted from a CT-based ED atlas by co-registering an MR image with the developed atlas [63]. In addition to enabling heterogeneous tissue representation, another major advantage of the method is that the pseudo-HU mapping and a possibility for organ contouring were implemented into an automatic workflow. Automation of pseudo-CT construction methods is important to enable routine clinical MRI-based RT. If adopting a pseudo-CT construction method requiring image co-registration in a clinic, the accuracy and reliability of the applied co-registration technique should be verified. Possible co-registration offsets could cause tissue misrepresentation in pseudo-CTs and systematic uncertainties in RT [63, 70, 71]. Precise heterogeneous tissue

representation and localization in pseudo-CTs could enable accurate and reliable dose calculation and image guidance.

Dose calculation accuracy in images with simplified tissue representation

Tissue inhomogeneities influence photon absorption and scattering, and thus simplified representations of body tissues reduce RTP dose calculation accuracy [1]. This has been concluded also by the previous investigations illustrating that dose calculation accuracy in pseudo-CTs can be improved by increasing heterogeneity of tissue representation [35-38, 59-70]. For prostate cancer patients, the reported MRI-based dose calculation accuracies compared to those in standard CTs have been within 4% in pseudo-CTs representing the entire body volume as water-equivalent, mostly within 2-3% in pseudo-CTs with additional bulk density segments, and within 2% in pseudo-CTs constructed either by the bone conversion technique or by the atlas-based ED mapping method [35-37, 60-64]. The results are encouraging for MRI-based RT in the pelvis, considering the dose calculation accuracy recommendations of 2-3% in realistic treatment situations [32-34]. On the other hand, previous examinations have not reached the 1% ultimate goal of dose calculation accuracy, have shown substantial dose calculation errors in organs-at-risk (OARs), and were not performed with Monte Carlo (MC) algorithms which are considered reference for all other dose calculation methods [1, 2, 33, 59, 72]. Conventional dose calculation algorithms employed for RTP include approximations about e.g. the influence of tissue inhomogeneities and scattering [1, 2].

If representing the soft tissue volume, or even the whole body, with an average homogeneous HU in a pseudo-CT, it can be assumed that this average value may be appropriate for some patients with certain treatment techniques, but this HU estimation would be insufficient for some individual anatomies, thus causing considerable dose calculation uncertainty for these patients. It is likely that dose distribution accuracy cannot be optimal in the entire body volume, such as in the OARs, although the dose might be averaging to nearly optimal for the target volume with some individual anatomies. Previous studies have neither evaluated dose distribution accuracy locally in the body volume nor addressed dose calculation accuracy for different-sized patients with varying tissue proportions.

The substantial differences between EDs of different bony tissues, ranging from those in high density bone cortex to those in low density core, may cause that the absorbed dose distal to a bone not necessarily correlate only with the physical thickness of the bone as it does if applying a modelled single HU for the bones in a pseudo-CT. A study examining in detail the effect of different bone parts to regional absorbed dose profiles of a single RT beam has not been conducted. This has not been investigated either by measurements or calculations, which would include also the examination of local calculation errors in pseudo-CTs. These investigations would be of particular value in one field treatments and also in increasingly applied intensity-modulated RT (IMRT) methods, in which a major part of the planned dose in a specific volume in target can be delivered from limited field directions due to healthy organ constraints.

Misrepresentation of tissue boundaries in pseudo-CTs could result in additional RTP uncertainty. In pseudo-CTs of the pelvis, especially the bone outline misrepresentation is possible due to the susceptibility-induced bone outline shift and perturbations, and if the bone-outline contouring is mandatory and not conducted precisely. The bone outline accuracy might be especially important with the bone conversion technique because under- or over-segmentation of bone outline could cause either substantial underestimation of the cortical bone HUs or major misrepresentation of the adjacent soft tissues, respectively. Previous studies have not evaluated the influence of bone outline errors on dose distribution [35-38, 59-66]. Relation between bone contouring precision and dose calculation accuracy could be determined to evaluate the feasibility of pseudo-CT construction methods for a routine clinical RTP workflow and to quantify acceptance limits for bone segmentation.

Possibilities for image guidance

The most reasonable method for conducting IGRT in MRI-based RT would be through automatic MR-to-MR image co-registration between the RTP- and the localization images. MRI-guided RT is currently available only in few clinics, which have either constructed a dedicated MRI-guided RT treatment facility or installed the MRI-^{60}Co system recently [22-24, 29, 30]. MRI-Linacs are not commercially available [25-28]. Consequently, it is likely that the X-ray -based localization methods will maintain their status as the most widely employed IGRT techniques in the near future.

Previous studies have suggested that IGRT with planar localization images could be conducted by relying merely on MRI by reconstructing the 2D reference DRRs from pseudo-CTs [36, 64, 65, 73, 74]. However, no previous work has demonstrated the feasibility of MRI-based patient position verification by following a standard clinical workflow such as achieving patient position corrections by co-registering the planar localization images and pseudo-DRRs. It would be especially reasonable to examine feasibility of MRI-based reference images for the increasingly applied IGRT technique achieving patient position corrections through automatic registration between the RTP images and CBCT localization images.

1.4 Aims of the study

There is a growing interest in RT community to include MRI into the RT workflow [16, 21, 31]. It can be expected that in the near future there will be an increase in the number of RT departments installing dedicated MR simulators and/or MRI-guided RT treatment platforms [16, 21, 31]. These clinics, and those already conducting MR simulations or MRI guidance, could find it particularly valuable to introduce methods enabling the entire RTP workflow by relying merely on MRI-based images. To quantify whether the MRI-based RTP workflow could be performed accurately according to the required standards of modern RT, it would be beneficial to conduct the related investigations with the state-of-the-art dose calculation and IGRT methods that are clinically available and widely adopted. To reach this goal, it could be

advantageous to enable construction of heterogeneous tissues-presentative pseudo-CTs of the pelvis from MRI data.

This work aimed to design an MRI-based RTP workflow for prostate cancer patients that could be conducted accurately according to the required standards of modern RT. The overall research objective could be broken down to four main research goals:

1) Developing a technique for construction of heterogeneous tissues-presentative pseudo-CT images of the pelvis based on image data obtained by a clinically available MRI sequence [II].
2) Determining dose calculation accuracy in these heterogeneous pseudo-CTs [I-III].
3) Measuring potential susceptibility-induced bone outline shift and geometric perturbations in MR images by applying a dedicated phantom, and evaluating the effect of bone outline errors on dose calculation accuracy in the pseudo-CTs [III].
4) Investigating whether IGRT with X-ray -based localization images could be performed with MRI-based reference images in the pelvis [IV].

Additionally, the study aimed to quantify uncertainties in the MRI-based RTP workflow compared to standard CT-based process, and to evaluate potential benefits of MRI-based RT with heterogeneous pseudo-CTs compared to using conventional homogeneous representations of body and bone volumes in the pseudo-CTs [I-IV].

2. Materials and Methods

2.1 MR and CT imaging

The CT and MR images employed in the present work were acquired by the RT simulators of Helsinki University Central Hospital (HUCH) Cancer Center. The patient imaging had been performed during the same day for each patient with both imaging modalities by following the clinical protocols and the general requirements of RT patient positioning [I-IV, 20]. The compact imaging protocol in the clinic has been designed to obtain essential information about patient anatomy for diagnostics and RTP, by exploiting the possibilities of MRI as a multi-parametric imaging modality for powerful integration of anatomical details [20]. Figure 1 presents the employed MR simulator 1.5 T imager GE Optima MR450w in HUCH Cancer Center. The scanner has a wide bore (Ø: 70 cm), and it is equipped with such accessories as a laser-localization system, MR-compatible fixation and a flat indexed table top to which a constructed receiver coil frame can be attached without patient body contact [I-IV, 20]. This section presents the applied processes for imaging and patient selection in this study.

Figure 1. The MR simulator in HUCH Cancer Center (2011). a) shows the scanner with the goal-post laser system, and b) presents patient positioning for pelvic imaging with MR-compatible immobilization. The anterior part of receiver coil is attached to the constructed frame, and posterior part of the coil is placed below the flat table top.

Applied MR and CT images

MRI was performed with T_1-weighted 2D SE, T_2-weighted 3D fast SE (FSE), and T_1/T_2*-weighted 3D dual echo fast GE (FGE) sequences [I-IV, 20]. Table 1 presents the applied MRI sequence parameters. The dual echo FGE sequence provides four images with the single acquisition, i.e. out-of-phase image (fat and water signals are out-of-phase, TE 2.1 ms), in-phase image (fat and water signals are in-phase, TE 4.2 ms), water-only image and fat-only image [75, 76]. The water and fat –only images are generated with the two-point Dixon method [75, 76]. With the dual echo FGE sequence, parallel imaging is applied to shorten acquisition time (<5 minutes with prostate cancer patients). The frequency encoding direction was posterior-anterior (PA), and 3D images were reconstructed axially. Geometrical distortion caused by nonlinearity of imaging gradients and signal intensity inhomogeneity of MR image series were corrected with vendor software (GradWarp3® [based on theoretical shape of image encoding gradient field spherical harmonic decomposition, 3D] and PURE® [phased array uniformity enhancement, multi-channel RF coil sensitivity normalization based on calibration series, 3D], respectively) [20, 21, 77-80]. Moreover, the DICOM headers of MR images were modified (set as CT) to ascertain capability of using MRI-based images with all employed RTP systems and software.

Table 1. The applied MRI sequences with their parameters.

Sequence	Name®	TE (ms)	TR (ms)	Flip angle (°)	Bandw. (kHz) [Hz/px]	FOV[a] (cm^2)	Acquis. matrix[a] (f. × p.)	Voxel size[ab] (mm^3)
T_1/T_2*–weighted 3D FGE	LAVA[c] Flex	2.1, 4.2	6.8	15	90.9 [425]	42 × 42	428 × 448	0.98 × 0.94 × 1.2
T_1–weighted 2D SE	T_1 SE	20	500	90	25 [156]	32 × 32	320 × 320	1 × 1 × 1
T_2–weighted 3D FSE	Cube	124	2000	90	62.5 [326]	37 × 37	384 × 320	0.96 × 1.16 × 1.2

[a] Imaging of the phantom (Section 2.2). In patient imaging the parameters may be adjusted.
[b] Slice thickness interpolated (e.g. 1.2 mm interpolated from 2.4 mm).
[c] Liver Acquisition with Volumetric Acceleration.

CT imaging was carried out with the 4-slice CT scanner GE LightSpeed RT (GE Medical Systems Inc., Waukesha, WI, USA). The simulator is subject to regular QA including HU-to-ED calibration with the RMI-phantom (Gammex, Middleton, WI, USA) [I-IV, 20]. The unit was operated at 120 kVp with 2.5 mm slice thickness (1.25 mm for phantom imaging), 50 cm × 50 cm field-of-view (FOV), and 512 × 512 matrix size (0.98 mm pixel size).

The CT and MR images of each patient were co-registered by a commercial medical image processing software (rigid registration relying on mutual information, MIM Software Inc., version 5.4, Cleveland, OH, USA), and both images were set in the coordinate system of the CT image [I-IV]. Visual inspection was conducted to verify optimal image co-registration of internal anatomy, i.e. further re-adjustments would have not improved the co-registration accuracy.

Patients

The study included 25 prostate cancer patients whose RTP had been conducted applying two imaging modalities: MRI for target delineation, and CT for dose calculation and image guidance. The study did not have any impact on treatment of these patients. The patients were selected retrospectively from the patient database of HUCH Cancer Center. First, 20 patients were randomly selected in order to form two groups: 10 for generation of conversion-based heterogeneous pseudo-CT construction technique (data collection group), and other 10 for pseudo-CT construction and testing of these images (test group) (Sections 2.3-2.5) [II]. The division of patients was performed by estimating the amount of subcutaneous fat in the pelvis, because different soft tissue proportions affect the MR signal and may thus limit the accuracies of the HU conversion and dose calculations in the constructed pseudo-CTs [II]. The patients were set in order according to the amount of subcutaneous fat, and every other patient was selected for the data collection group, and every other for the test group to ensure appropriate patient heterogeneity within both groups [II].

The patients in the test group were divided into three sub-groups according to the used localization imaging method (Section 2.5: kV CBCT, kV planar or MV planar localization). In order to obtain 5 patients for each sub-group, 5 other test patients were selected for the study based on the employed localization imaging method. These 5 patients were included also into the dose calculation investigation in addition to the 10 previously selected test patients (Section 2.4). The clinical target volume (CTV) of each patient included the prostate and the seminal vesicles.

2.2 Determination of bone outline accuracy in MR images

A measurement procedure for the potential susceptibility-induced bone outline shift and geometric perturbations was developed to complement the previous research on geometrical distortion with the MR scanner 1.5 T imager GE Optima MR450w [III, 20]. The patient imaging workflow and parameters introduced in Section 2.1 were adopted for the phantom imaging [I-IV, 20]. This section describes the phantom construction and the bone outline measurements.

Bone and gelatine phantom

To evaluate the bone outline accuracy in the images with respect to actual physical bone outline locations, and to conduct the research with patient-like materials, a dedicated phantom was constructed by using fresh bones of a wild deer and gelatine made out of pig skin [I, III]. The author affirms that the reported research was conducted in accordance with the ethical policies of HUCH. Figure 2 presents the phantom with its construction schematics (the phantom was designed to enable also examinations on dose distribution behind the bones, Section 2.4). Figure 3 illustrates the bone contrast in the obtained phantom images [I, III]. The fat-only image achieved

by the dual FGE sequence was excluded from the investigation, because the image contrast enables no reliable visual bone outline localization and segmentation.

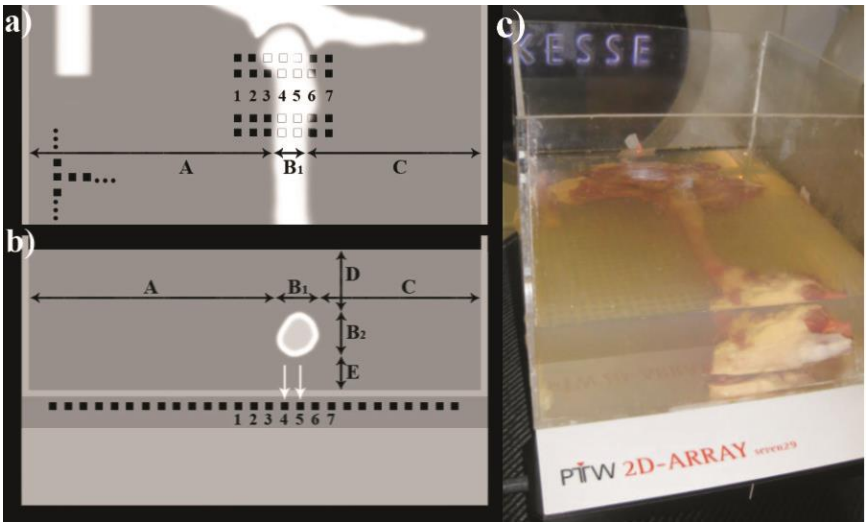

Figure 2. The constructed bone and gelatine phantom. a) and b) present the construction schematics of the phantom: a) illustrates a part of the structure from above; femur, femoral head and pelvis in the middle, and a part of the tibia at top left, and b) illustrates transversal slice at femur position. Letters from A to E represent the analyzed distances of bone outline location measurements. Numbers 1-7 show the ionization chambers that were of interest, from which the most important dose measurement positions behind the bone are shown by white arrows (Section 2.4). c) shows the phantom positioned for the dose measurements.

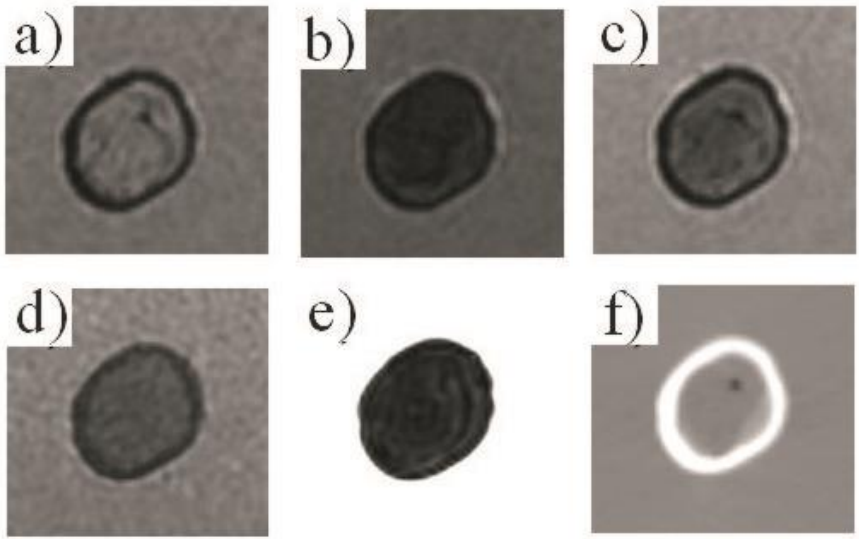

Figure 3. Example transversal images of the deer femoral bone positioned in the gelatine; a) T_1/T_2*-weighted FGE in-phase, b) T_1/T_2*-weighted FGE out-of-phase, c) T_1/T_2*-weighted FGE water-only, d) T_1-weighted SE, e) T_2-weighted FSE, and f) CT.

The bone structure included the fresh deer back leg bones from the pelvis to the tibia with the maximum bone diameters of approximately 5.5 cm, 3.0 cm and 2.0 cm to the femoral head (including the greater trochanter), the femur and the tibia, respectively. The femur and the tibia were composed of a medullary cavity and an exterior cortical bone layer of ~3 mm [I, III]. Before examinations, the soft tissues located exteriorly to the bone cortex were removed without damaging the bone surface and the bones were attached into a 30×35×20 cm^3 PMMA box [I, III]. The femur direction was parallel to the longitudinal imaging direction. The femur edge was ~1.5 cm lateral to the box middle axis, ~2 cm above the bottom. Part of the tibia was positioned 12 cm lateral to the middle axis. The box was filled with a mix of 8 l of warm water and 400 g of pig skin -based gelatine, so that all of the bones were covered with the liquid by at least a couple of centimeters. The gelatine was solidified by placing the box in a refrigerator. Predefined locations for the upcoming measurements were marked onto the box walls with laxative pills. The ionization chamber (IC) matrix (2D-Array seven29, PTW Freiburg GmbH, Germany) was located underneath the box together with 5 cm of water-equivalent material (RW3, PTW Freiburg GmbH, Germany) under the detector.

Measurements for the bone diameter and outline location

The accuracy of the bone edge location and the bone diameter in the MR images were evaluated by comparing the measured pixel-based distances with the actual physical measurements of the phantom [III]. CT image was also included into the examinations to evaluate whether the bone outline location accuracy in the CT is substantially superior compared to that in the MR images. The bone diameter and the distances from the bone edges to the phantom walls were measured to both phase- (lateral) and frequency (vertical) MRI encoding directions (Figure 2) [III]. Additionally, the examinations were designed to take into account errors in the sums of the distances, which could have revealed whether the possible errors in the distances were compensated for, or whether they accumulated, thereby causing amplified errors. The measurements were performed at four predefined locations. Three of the locations included the femur within ±2 cm from the magnet isocenter and one included the tibia 12 cm lateral from the magnet isocenter (Figure 2). The physical measurements were taken by using a caliper and dipsticks. The corresponding distances in the images were measured with a RTP system (Eclipse® 10.0, Varian Medical Systems Inc., Helsinki, Finland). With each image series the criterion for the bone edge was determined by measuring the pixel values representing the cortical bone and those representing the gelatine, and setting a threshold pixel-value in between. By considering the image pixel size and the intended segmentation accuracy for RTP, both physical and image-based measurements were rounded to the nearest 0.5 mm [III].

2.3 Generation of pseudo-HU information from MRI data

A possibility to develop a method to obtain heterogeneous tissues-presentative pseudo-CTs of the pelvis from MRI data of a single MR image series was investigated for the T_1/T_2*-weighted in-phase MR image [II]. The sequence was applied to the task

because it provides important bone characteristics, T_2* correlates with the bone density, and the image contrast enables clear separation of different tissues (e.g. the bone outlines and its surroundings) [II, 1, 17, 18, 64, 81-84]. The MR signal is derived from several tissue components within a voxel and is an integral over different values of such as proton density (PD), T_1 and T_2* [64]. The MR signal is influenced also by such as susceptibility effects and geometry. Consequently, the relation between the MR image intensity values and electron densities is complex. This section describes the examinations evaluating the relation between the intensity values of the T_1/T_2*-weighted in-phase MR image and the CT image HUs particularly for each tissue, and introduces the dual model pseudo-HU conversion technique for heterogeneous pseudo-CT construction in the pelvis.

Generation of soft tissue conversion model outside of bone segment

The relation between the T_1/T_2*-weighted in-phase MR image intensity values and the standard CT image HUs of the pelvic soft tissues was analyzed to evaluate a possibility to construct a soft tissue pseudo-HU conversion model. The data collection was conducted by volumes-of-interest (VOIs) placed into different tissues all over the image series of the 10 variable-sized prostate cancer patients selected based on different tissue proportions in the pelvis (Section 2.1) [II]. Figure 4 shows an example of the data collection. The examination was conducted with one thousand 5-mm-diameter circular (65 mm^3) VOIs from which the mean voxel-values in both images were collected to minimize the uncertainty caused by image co-registration and Gaussian noise that could interfere with voxel-by-voxel examinations. Additionally, so-called assessment-VOIs were selected by setting lines of VOIs from body outline to the image center to examine average HU profiles of soft tissues radiation beam traversing through in external RT [II]. Within these assessment-VOI lines, also pixel-by-pixel mapping was conducted with 5-mm spacing. These pixel values together with the assessment-VOIs helped in evaluating the relation between HUs and MR image intensity values at tissue boundaries and in recognizing uncertainty of conversion model construction caused by image co-registration errors, noise and partial volume effects in 5-mm-diameter VOIs [II].

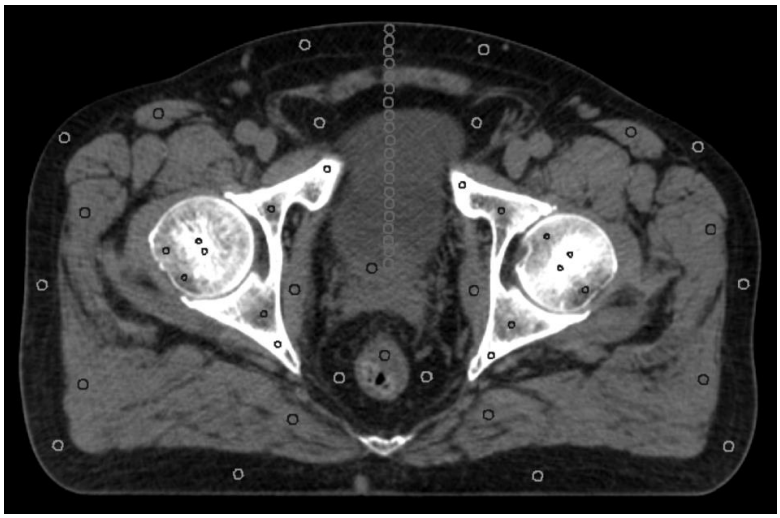

Figure 4. An example of the VOI-selection from different tissues in a transversal CT slice. The circles illustrate the VOIs placed in different soft- and bony tissues.

The soft tissue HU conversion model was constructed by dividing the MR image intensity scale into threshold-based sections representing signals from urine, muscle and fat. MR signals below the maximum intensity value of the urine-VOIs were regarded as urine, MR signals within standard deviation (SD) of muscle-VOIs (from average – SD to average + SD) were set as muscle, and all MR image intensity values above the SD (average – SD) of fat-VOIs were considered fat [II]. Each of these MR image intensity sections was converted into VOI-based average HU of the tissue that the MR image intensity section presented. MR image intensity values between those presenting urine, muscle and fat were converted into HUs with linear interpolation. The model was generated by adopting the structure-based SDs and by including the interpolation between the thresholds in order to present correctly also the voxels at tissue boundaries and to construct an appropriate model functioning with all patients (differences in absolute intensity levels between the images) without need for patient-specific adjustments, such as MR signal normalization [II].

MR signals from different bony tissues and enhancement of bone conversion model

The bone conversion technique suggested by Kapanen & Tenhunen relies on a simplified model about the relation between intensity values of the T_1/T_2*-weighted in-phase MR image and HUs [64]. The MR signal is normalized by an average intensity value of the muscle tissues adjacent to the iliac bones for each patient to minimize inter-patient variations in absolute intensity level [64]. The normalized MR signal can be presented by the equation:

$$s = \iiint \frac{A[T_1(x,y,z)]}{A_{muscle}} \frac{P(x,y,z)}{P_{muscle}} e^{-TE\cdot\left[R_2^*(x,y,z)-R_{2\,muscle}^*\right]} \rho(x,y,z)\cdot dx\cdot dy\cdot dz \qquad (1)$$

where R_2*is $1/T_2$*, P is PD, A is a T_1-dependent factor determined by the flip angle, TR and level of spoiling of transversal magnetization, and $\rho(x,y,z)\cdot dx\cdot dy\cdot dz$ is the

fraction of a component having PD, T_1, and T_2* within a voxel at location x,y,z. [64]. The conversion from the normalized MR image intensity values into pseudo-HUs was obtained by applying a scanner-specific second order polynomial fit within the contoured bones, and realized by dividing the intensity scale into sub-groups [64].

In this work, the relation between the T_1/T_2*-weighted in-phase MR image intensity values and CT image HUs was investigated particularly for different bony tissues [II]. Figure 4 shows also an example of this VOI-based data collection from the cortical bone, the bone marrow, and dense/low-dense parts of the spongy bone of the 10 data collection patients (Section 2.1). Although the dark appearing bone cortex is clearly distinguishable from its surroundings in the adopted MR images, the detected MR signal from the cortical bone cannot be assumed genuine with the applied imaging sequence (TE >> T_2*) [II, 64, 85, 86]. To evaluate origins of the intensity values representing the cortical bone and to demonstrate uncertainties related to the low signal levels with the applied imaging sequence the noise level was evaluated in the patient MR images by measuring intensity values in the air [II].

The MR signals from low density bony tissues may vary considerably between patients due to variations in bone marrow anatomy, such as proportions of fat and water in this tissue, although the HUs of these tissues are relatively constant (~0 HU) [56-58, 87]. Thus, the previously suggested bone conversion model was modified by introducing a patient-specific cut-off MR image intensity value aiming to adjust the model to present the low density bony tissues precisely [II, 64]. The cut-off value was determined individually for each patient by patient-specific mean value of two VOIs from low-density parts of both femoral heads that are mostly composed of bone marrow. The MR image intensity values above this cut-off limit were assigned to 0 HU.

Implementation of dual model pseudo-HU conversion technique

The generated soft tissue- and the enhanced bone conversion models were connected to form a dual model pseudo-HU conversion technique [II]. The method was implemented by constructing an automatic pseudo-HU conversion workflow into a commercial medical image processing software (MIM®), and by generating heterogeneous pseudo-CTs for 15 variable-sized prostate cancer patients (Section 2.1) [II-IV]. The bone conversion model was applied within manually precisely contoured bones by means of the patient-specific adjustments described earlier in this Section, and the soft tissue conversion model was applied to MRI voxels located between the bone- and body outline contours [II-IV]. The conversion models were employed by dividing the MR image intensity range into steps of ~20 each [II].

The image quality of the pseudo-CTs was examined by means of VOI-based analysis similar to those used for generation of the models [II]. Here, the HUs in pseudo-CTs were compared to the corresponding HUs in the standard CTs, both in soft- and bony tissues. Additionally, the potential improvement in pseudo-HU profile accuracy when applying the soft tissue conversion model instead of the assumed water-equivalence

for soft tissues was evaluated with statistical hypothesis tests (paired t-test and one-tailed F-test: $p \leq 0.05$ were considered significant) [II].

2.4 Dose calculation

Dose calculation accuracy in the heterogeneous pseudo-CTs obtained by the dual model pseudo-HU conversion technique introduced in Section 2.3 was quantified for 15 prostate cancer patients (Section 2.1) [II, III]. Possible regional dose inconsistencies in the pseudo-CTs were investigated particularly behind the bones by using the dedicated bone and gelatine phantom presented in Section 2.2 [III]. The phrase "behind bones" in this work refers to the absorbed dose in material distal to the bone in the direction of the central axis of a single radiation field. This section describes the examinations conducted to quantify the dose distribution accuracy in the pseudo-CTs.

Dose calculation in heterogeneous pseudo-CTs of prostate cancer patients

Dose distributions in the prostate patient heterogeneous pseudo-CTs were analyzed for 360° volumetric-modulated arc therapy (VMAT) and 7-field IMRT treatment plans with 6 MV photons [II, III]. These plans were calculated in standard CTs, and then copied and re-calculated with equivalent monitor units (MUs) in the pseudo-CTs by the X-ray Voxel MC algorithm (XVMC, version 1.6, Monaco® 3.20, Elekta AB, Stockholm, Sweden) for the VMAT plans, and with the anisotropic analytical algorithm (AAA, Eclipse® 11.0) for the IMRT plans [II, III, 72, 88, 89].

The body and planning target volume (PTV) in standard CT were applied for all images in order to minimize uncertainties in dose distribution comparisons between the images stemming from patient position differences and from potential minor CT-to-MR image co-registration errors [II, III]. The volumes in which the patient body in MR image unfilled the body in CT were assigned to water-equivalent, and the volumes in which patient body in MR image was exterior to the body outline in CT were set to air-equivalent.

The dose calculation accuracy in the pseudo-CTs was determined by comparing the PTV and OARs (the rectum and the bladder) dose-volume-histogram (DVH) parameters in the pseudo-CTs with those in standard CTs [II, III]. Dose distribution differences in the pelvis were evaluated locally by adopting the 2D gamma index method with dose evaluation software (VeriSoft 4.1, PTW Freiburg GmbH, Germany) [II, III, 90].

The influence of bone segmentation accuracy on dose distribution in the heterogeneous pseudo-CTs was also evaluated [III]. For these investigations the bone contours in MR images were intently expanded or contracted with 1 mm spacing and the pseudo-CTs were constructed individually for each patient with each of the bone

segments by the dual model pseudo-HU conversion technique [III]. The treatment plans were re-calculated also in each of these pseudo-CTs.

The treatment plans were calculated also in simplified pseudo-CTs to evaluate potential benefits of the full heterogeneous pseudo-CT on dose calculation accuracy in MRI-based RT. The two other employed pseudo-CT images were: 1) bones-only conversion -based pseudo-CT, and 2) bulk pseudo-CT, in which the bone segment was assigned to represent the average HU of bones: 330 [I-IV, 35, 57, 64]. For both types of pseudo-CTs all the tissues outside bone segment were assigned to water-equivalent [I-IV, 35, 57, 64]. The statistical hypothesis tests were conducted to examine whether error averages (paired t-test) and, more importantly, whether error variances (one-tailed F-test) in dose distributions (gamma index passed points and PTV DVH-parameters) decreased significantly ($p \leq 0.05$) when employing soft tissue conversion in the pseudo-CTs instead of homogeneous representation of these tissues.

Dose level behind different bone parts

A phantom examination was performed to quantify the magnitude of possible regional deviations in dose distribution behind the bones when the dose is calculated in pseudo-CTs and to determine the effect of different bone parts on the absorbed dose profile in tissue behind the them [I]. Dose level measurements were conducted to evaluate clinically detectable dose level deviations behind different bone parts. The measurements were considered beneficial also to demonstrate proper utilization of the image data and to ascertain appropriate configuration of the calculation algorithms for clinical situations.

The absorbed doses were measured with the IC matrix detector (PTW®, IC Ø: 5 mm, IC center-to-center distances: 10 mm, measurement accuracy: 0.2%) [I, 91]. The dose evaluation level was at a depth of 9.6 cm from gelatine surface ~3 cm behind the bones. The phantom was irradiated to 100 MUs with an open 9.6 cm by 10.4 cm RT field from a gantry angle of 0° at the nominal photon energies of 6 MV and 15 MV. In order to set radiation to traverse through the femur and the femoral head, the field isocenter was set laterally/longitudinally to the middle of an IC, which was located behind the femur edge, and vertically on top of the detectors (Figure 2). The phantom position was confirmed with kV CBCT system that is integrated with the gantry of linear accelerator (XVI® integrated with Elekta Axesse®) [I, IV, 11, 91]. The effect of the bones to the absorbed dose was evaluated by calculating local dose differences between the doses behind bones and those obtained with a similar field irradiated through gelatine only to eliminate the influence of field shape on the evaluations. The dose differences were calculated with dose evaluation software (VeriSoft®) by the equation:

$$\Delta_D = \frac{D_b - D_{ref}}{D_{ref}} \cdot 100\% \qquad (2)$$

where Δ_D was the dose difference, D_b was the dose with the field traversing through the bones and D_{ref} was the dose using the reference field through gelatine only [I]. Dose difference profiles were investigated in the lateral direction perpendicularly to the longitudinal axis of the bone behind the femur and the femoral head with the greater trochanter [I]. Special interest was focused on the ICs positioned entirely behind the bones (Figure 2).

Dose calculation deviations in the bone conversion- and in the bulk pseudo-CTs behind the bones were quantified by comparing the calculation results with those obtained in the standard CT of the phantom [I]. The calculations were performed with the XVMC and the superposition algorithms (Monaco® 3.00 and XiO® 4.60, respectively, Elekta) by using the same field arrangements and dose evaluation level as those in the measurements (calculation grid: 1 mm) [I, 72].

2.5 Image guidance

Feasibility of conducting IGRT in the pelvis with MRI-based reference images was evaluated for two widely used X-ray -based localization methods: 1) automatic localization with CBCTs, and 2) manual localization with planar images [IV]. This section introduces the tested reference images, and describes the methods applied for evaluating the patient positioning accuracy with the MRI-based reference images.

IGRT with localization CBCT and automatic position verification method

The 3D localization images were obtained by the kV CBCT system XVI® integrated with Elekta Axesse® providing patient position corrections by automatic grey-value or bone rigid registration (based on grey level correlation ratio or chamfer matching algorithm, respectively) between localization CBCT and reference CT within user specified VOI (either a cubic-shaped "ClipBox" or a contour-shaped "Mask") [IV, 11-13, 91-95]. Visual inspection is required to detect potential outliers (i.e. registrations that have clearly failed, but the system has not reported any warnings) and to verify the registration result before performing patient position corrections [IV, 12, 13, 91-95].

In this work, the T_1/T_2*-weighted in-phase MR, the heterogeneous pseudo-CT and the bulk pseudo-CT images were assigned as reference against localization CBCTs (50 scans with image voxel size of $1\times1\times1$ mm^3, 5 prostate cancer patients), and the bone- and grey-value registrations were performed separately for each image pair [IV]. The feasibility of the reference images for automatic registration was evaluated with a 10-cm-diameter "ClipBox" VOI positioned to the isocenter. The VOI size was chosen to cover also tissues surrounding the moving organs. Additionally, the automatic registrations were performed based on the current position of the prostate and the seminal vesicles (CTV+5mm "Mask" VOI) [IV, 12, 13]. The position corrections obtained by automatic registration between each MRI-based reference image and localization CBCT were compared to those obtained by applying standard reference

CT. In this study, the contribution of major registration outliers to the results was decreased as follows; the registration differences were calculated with all the registrations, and based on these results, the registrations with >3 SD difference in any direction were excluded, and the registration differences were recalculated without these (>3 SD) major outliers. The recalculated averages and SDs were reported.

Reconstruction of pseudo-DRRs and IGRT with 2D localization images

Reference DRRs were reconstructed for 10 prostate cancer patients for whom image guidance had been conducted relying on 2D planar localization [IV]. The reconstruction was conducted in PA and in right-left (RL) directions from 3D image information of HUs over 100 (clinical protocol of HUCH Cancer Center). Heterogeneous pseudo-CT, bulk pseudo-CT and standard CT of each patient were applied for the DRR reconstruction separately.

The feasibility of the reference pseudo-DRRs for IGRT with planar 100 kV or 6 MV localization images (On-board Imager® or PortalVision®, respectively, Varian Medical Systems) was evaluated by manual 2D image registrations (Intuity®, XVI® R4.5 software, Elekta) relying solely on bony tissue presentation in the images [IV]. Ten clinical physicists performed registrations in three degrees-of-freedom between the localization images and each of the reference DRRs (one pair of localization images of each patient). The observers were blind to the resulting patient position corrections, from which those obtained with the pseudo-DRRs were compared to those achieved with the standard CT-DRRs. Statistical hypothesis tests (paired t-test and two-tailed F-test) were conducted to evaluate whether the position corrections with either heterogeneous- or bulk pseudo-DRRs were significantly ($p \leq 0.05$) more similar to those achieved with CT-DRRs than with the other. Additionally, the quality of the pseudo-DRRs was evaluated with three image similarity metrics to quantify whether the image quality in either type of pseudo-DRRs was significantly more similar to CT-DRRs than in the other [IV]. Table 2 presents a summary of the conducted investigations with the images employed in the present work.

Table 2. Summary of the investigations and the images used (X) in this study.

	The images employed in the investigations						
Investigation	MRI[a]	In-phase MRI[b]	Heterogeneous[c] pseudo-CT	Bone conversion[d] pseudo-CT	Bulk[e] pseudo-CT	Water-equivalent pseudo-CT	CT
Bone outline accuracy in the images	X	X	-	-	-	-	X
Development of pseudo-HU conversion	-	X	-	-	-	-	X
HU accuracy in pseudo-CT images	-	-	X	X	X	X	X
Dose distribution behind bones	-	-	-	X	X	X	X
Dose distribution in the pelvis	-	-	X	X	X	-	X
IGRT with CBCT localization	-	X	X	-	X	-	X
IGRT with 2D planar localization	-	-	X[f]	-	X[g]	-	X[h]

[a] T_1/T_2*-weighted FGE, T_1-weighted SE and T_2-weighted FSE images.
[b] T_1/T_2*-weighted in-phase MR image series obtained by a dual FGE sequence.
[c] Constructed by the dual model pseudo-HU conversion technique introduced in this work.
[d] Constructed by HU conversion of bones only (exterior to bone segment set as water-equivalent).
[e] Constructed by an average bulk HU of bones (exterior to bone segment set as water-equivalent).
[f] Heterogeneous pseudo-DRR reconstructed from the heterogeneous pseudo-CT image series.
[g] Bulk pseudo-DRR reconstructed from the bulk pseudo-CT image series.
[h] CT-DRR reconstructed from the standard CT image series.

3. Results

3.1 Spatial accuracy of bone outline in the images

Figure 5 illustrates the spatial accuracy of bone outline presentation in the images [III]. The determined bone diameter in the MR images was always within 1.0 mm compared to the physically measured diameter. In the distances from the bone edges to the phantom walls the maximum errors were 1.5 mm, which were obtained at 2 of the 80 measurements (with T_1 SE and T_2 FSE; distance D shown in Figure 2).

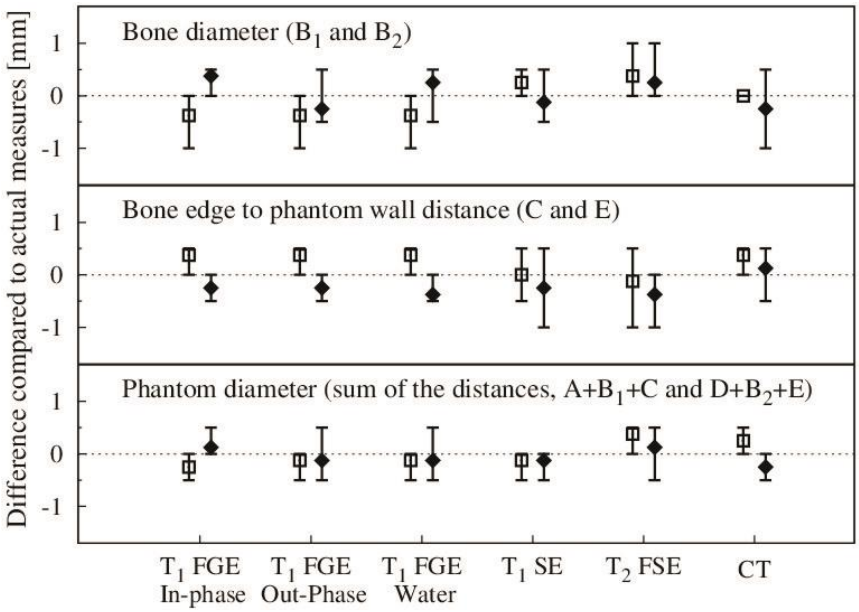

Figure 5. Differences between the actual physical measurements and the measured distances from each of the image series for the bone outline. Symbols and error bars illustrate averages and ranges of the differences, respectively (open symbols in phase- and solid symbols in frequency encoding direction). The letters represent the investigated distances shown in Figure 2.

3.2 Pseudo-HU conversion from MRI data and obtained images

Conversion models for soft- and bony tissues

Figures 6 and 7 present the soft- and bony tissue conversion models, respectively, which were connected to form the dual model pseudo-HU conversion technique [II]. The data collection from each examined soft tissue in Figure 6 (a) shows that MR image intensity values from urine, muscle and fat can clearly be separated from each other [II]. The conversion model was formulated as follows; the MR image intensity values below 112 were converted into the VOI-based average HU value of urine (8), the intensity values between 150 and 212 were assigned to the obtained average HU of muscle (55), and the intensity values above 346 were set as the average HU of fat (-104). The model converted the MR image intensity values from 113 to 149 and from 213 to 345 into HUs by means of linear interpolation.

The data collection from different bony tissues in Figure 7 (a) shows that MR signal range from bone marrow (SD from 288 to 410) was wide with a narrow HU range (SD from -42 to 44) [II]. The MR signal SD level in spongy bone was from 226 to 293 and from 317 to 436 in dense and low density parts, respectively, enabling appropriate determination of the cut-off value [II]. The MR image intensity values presenting the cortical bone showed only a relatively narrow range (SD from 73 to 136), although the HU range was wide (SD from 967 to 1391) [II]. The VOI-based cortical bone MR image intensity values were mostly higher compared to the estimated mean background noise in the images (ranging from 48 to 70 for 10 patients) [II].

Heterogeneous pseudo-CTs and HU accuracy in the images

The implemented automatic image transformation from MR image to pseudo-CT by the introduced dual model conversion technique can be found online as a video-clip [III]. Figures 8 and 9 illustrate examples of the obtained heterogeneous pseudo-CTs [II-IV]. For each patient, the soft- and bony tissue -based VOI-value average differences between HUs in standard CTs and in the pseudo-CTs ranged from -2 to 5 HUs in the soft tissues, and from 22 to 78 HUs in the bones [II]. The mean, SD and maximum local absolute value differences, i.e. HU uncertainties, were 11, 8 and 97 HUs in the soft tissues and 99, 100 and 522 HUs in the bony tissues, respectively. HU accuracy criterion of 20 HUs in the soft tissues and 200 HUs in the bony tissues were passed on average by 87% and 85% of the examined VOIs, respectively [II]. Examination of each tissue separately revealed that the highest average uncertainty in soft tissues was found in the muscle (12 HUs), and in bony tissues in the cortical bone (164 HUs) [II]. The soft tissue HU profiles were -13 and -12 HUs on average with ranges from -33 to 7 HUs and from -28 to 6 HUs in CTs and in the pseudo-CTs, respectively. The HU profile accuracy improved significantly (p=0.01) by using the soft tissue conversion instead of representing these tissues with homogeneous volume in the pseudo-CTs [II].

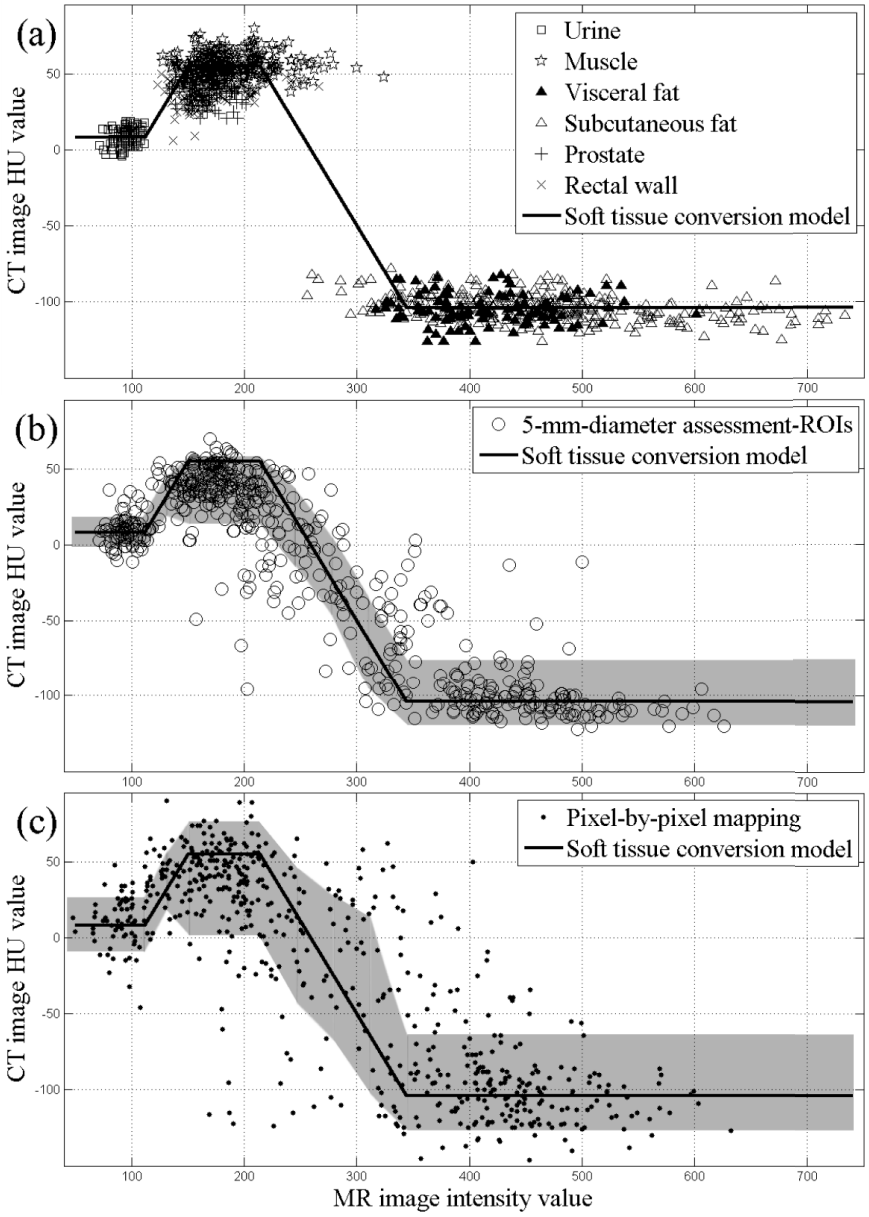

Figure 6. The corresponding soft tissue HUs for the MR image intensity values in the male pelvis and the introduced pseudo-HU conversion model for soft tissues. (a) presents the VOIs that were selected from different soft tissues and used for the model construction, (b) shows the assessment-VOIs that were collected as lines of VOIs from the body outline to the center of transversal image slices, and (c) illustrates the pixel-by-pixel mapping within the lines of assessment-VOIs. The grey areas in (b) and (c) demonstrate the HU SD levels of the collected assessment data in each Figure. The SD levels were calculated separately for the flat HU sections of the conversion model (MR intensity values below 112, from 150 to 212, and above 346) and for the linear interpolation sections (the section from 213 to 345 was divided into 3 segments). The SD levels are not precisely symmetric about the conversion model, because the assessment data were collected from different locations compared to the data used for model construction.

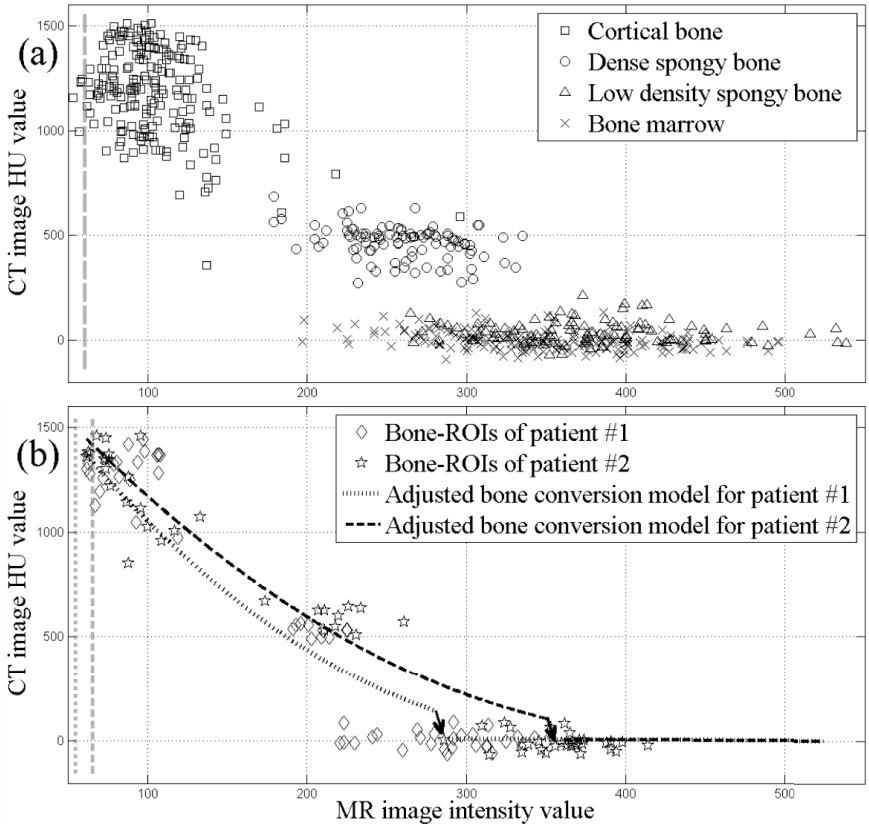

Figure 7. The corresponding bony-tissue HUs for the MR image intensity values in the male pelvis, examples of the adjustable pseudo-HU conversion model for bones and estimated average noise levels in the MR images. (a) illustrates the collected bone-VOIs, (b) demonstrates two example patient cases of the predictive bony tissue conversion model adjusted by patient-specific normalization factors (patient #1: 165, and #2: 195) and cut-off values (patient #1: 280, and #2: 350). The individual parameters aim to adjust the model for optimal pseudo-HU conversion of each patient's MR image series. The grey dashed vertical lines illustrate the estimated mean noise levels in the MR images; the line in (a) shows the average noise level of all patients in the data collection group and the lines in (b) represent the estimated mean noise levels in the example patient cases.

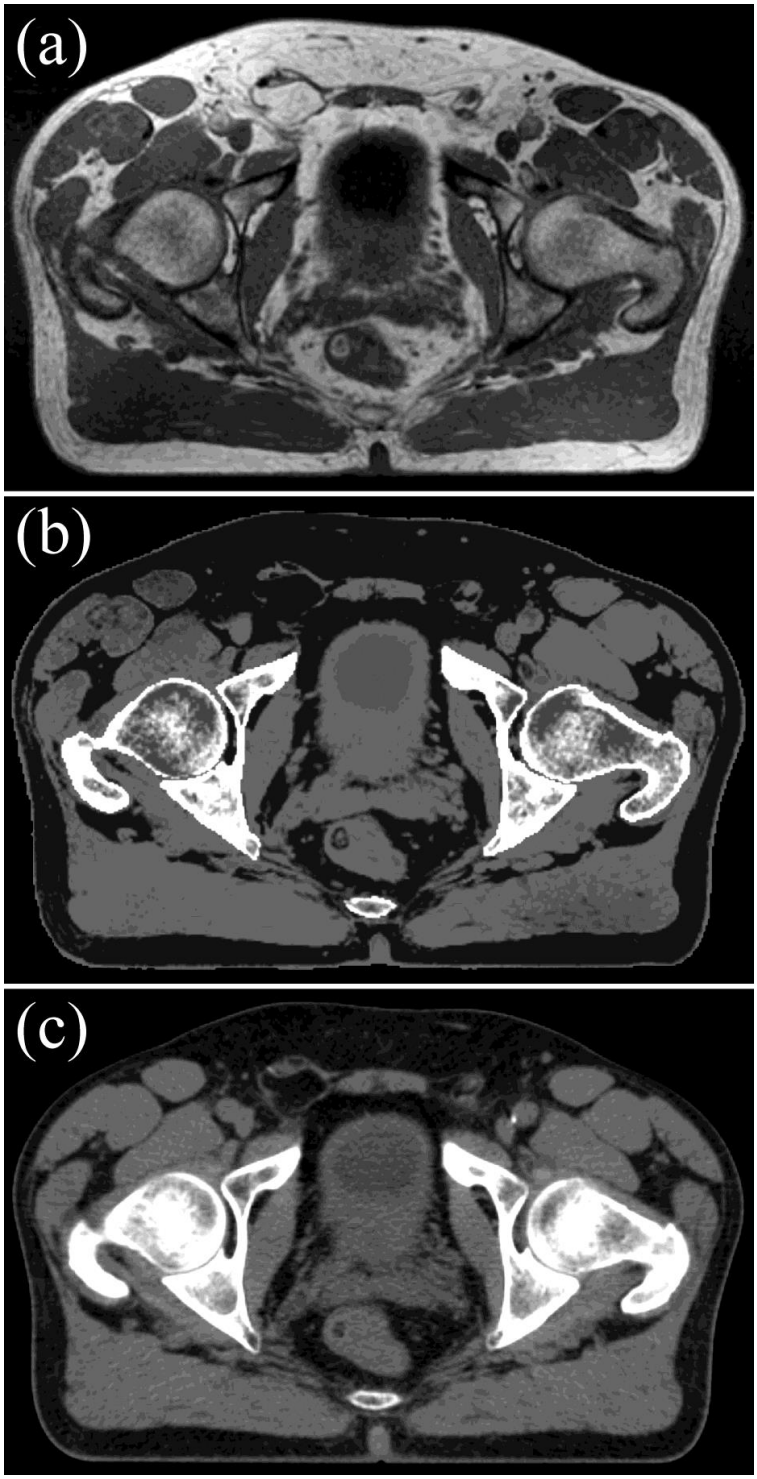

Figure 8. An example of a heterogeneous pseudo-CT (b) with the original MR image (a) from which the pseudo-CT was constructed by the dual model pseudo-HU conversion teshnique. The corresponding transversal slice of standard CT is shown in (c). Contrast in the images is not perfectly comparable (different windowing properties and scaling).

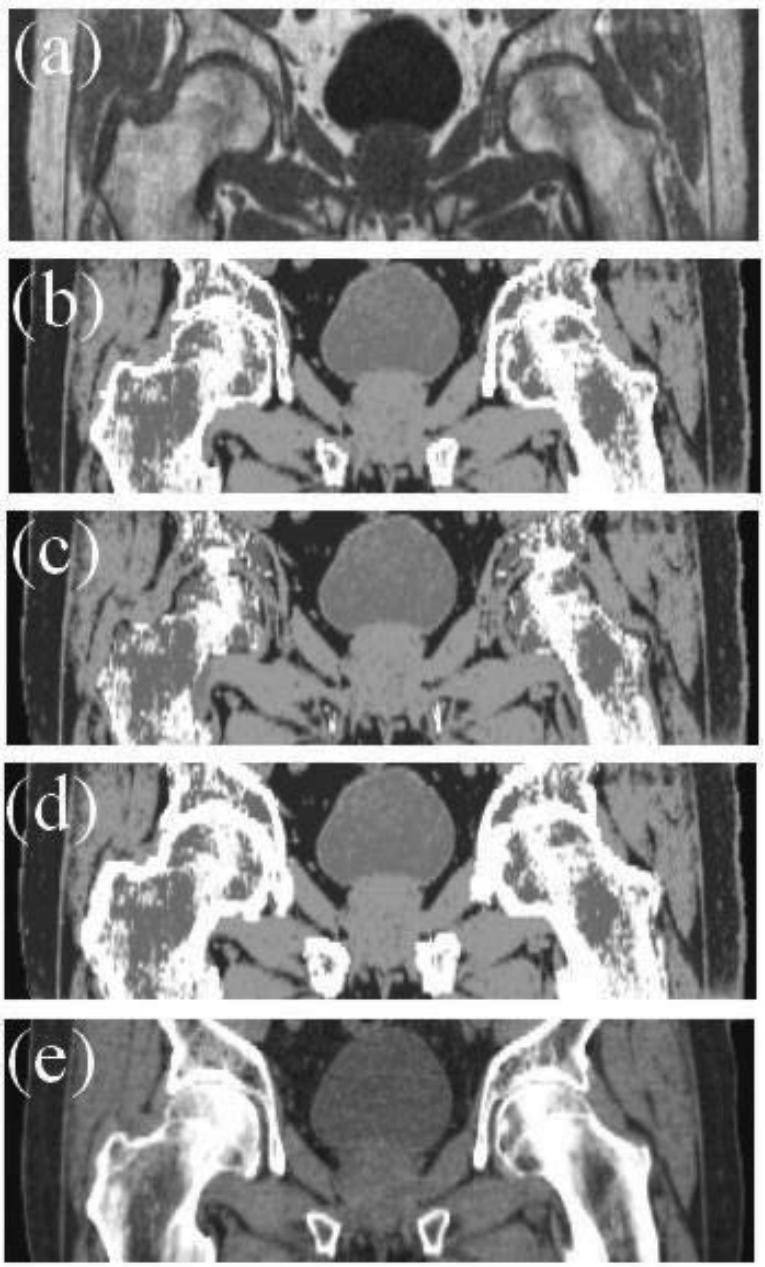

Figure 9. Example coronal views of the heterogeneous pseudo-CTs obtained by the dual model pseudo-HU conversion technique with precise (b), 3 mm too narrow (c), and 3 mm too wide (d) bone segments demonstrating the influence of segmentation errors to the generated pseudo-CT image. The original MR image and the corresponding CT image are shown in (a) and (e), respectively. Contrast in the images is not perfectly comparable (different windowing properties and scaling).

3.3 Dose distributions in pseudo-CT images

Dose calculation accuracy for prostate cancer patients

Table 3 presents the prostate PTV DVH parameter differences between the dose distributions in the standard CTs and those in the heterogeneous pseudo-CTs obtained either with the precise- or the systematically inaccurate bone segments [II, III]. Figure 10 and Table 4 show the dose distribution comparisons with the gamma index method [II, III, 90]. The maximum amounts of failed dose points (ranging up to 21% with 1% & 1 mm criteria) were detected in transversal image slices including as many pelvic bones as possible. At this image slice level the average percentages of dose points passing the local 1% & 1 mm (2% & 2 mm) criteria were 88% (99%) in the VMAT plans, and 98% (100%) in the IMRT plans [II, III]. The PTV mean dose level inconsistencies were on average (and in the worst cases) -0.2% (-1.0%–0.7%) and 0.0% (-0.7%–0.8%) in VMAT and in IMRT plans, respectively [II, III]. The OAR DVH parameter differences were detectable mainly only in high dose volumes, in which the differences were similar with those quantified for the PTV. With heterogeneous pseudo-CTs constructed by additional systematic bone segmentation errors of -3 mm, -2 mm, … , +3 mm the PTV mean dose level inconsistencies were up to 2.1%, 1.8%, 1.2%, -1.3%, -1.8% and -2.2%, respectively [III]. The average dose levels of PTV in the bones-only conversion -based pseudo-CTs and in the bulk pseudo-CTs were up to 2.3% and 2.6%, respectively, different compared to those achieved in the standard CTs. The dose calculation accuracy was significantly lower in the pseudo-CTs with homogeneous tissue representations compared to that in the heterogeneous pseudo-CTs [II].

Table 3. The prostate PTV dose consistency (%) between CTs and the heterogeneous pseudo-CTs[a] with variable-sized bone segments for 15 patients as mean ±SD (range).

		Additional systematic error in bone segment				
Plan	DVH (%)	-2 mm	-1 mm	0 mm	+1 mm	+2 mm
VMAT[b]	95	0.5 ±0.6 (-0.5–1.4)	0.1 ±0.6 (-0.7–0.9)	-0.3 ±0.6 (-1.1–0.6)	-0.6 ±0.5 (-1.3–0.3)	-1.0 ±0.6 (-2.0–-0.1)
	50	0.5 ±0.6 (-0.4–1.4)	0.1 ±0.6 (-0.7–0.9)	-0.3 ±0.6 (-1.0–0.7)	-0.6 ±0.6 (-1.3–0.4)	-0.9 ±0.6 (-1.8–0.0)
	5	0.5 ±0.6 (-0.5–1.5)	0.1 ±0.6 (-0.8–1.0)	-0.2 ±0.6 (-0.9–0.7)	-0.5 ±0.6 (-1.2–0.4)	-0.9 ±0.6 (-1.6–0.0)
IMRT[c]	95	0.9 ±0.4 (0.3–1.5)	0.4 ±0.4 (-0.3–1.0)	0.0 ±0.4 (-0.7–0.6)	-0.3 ±0.5 (-1.1–0.4)	-0.8 ±0.5 (-1.7–0.0)
	50	1.0 ±0.5 (0.3–1.7)	0.4 ±0.5 (-0.3–1.1)	0.0 ±0.5 (-0.8–0.7)	-0.4 ±0.5 (-1.2–0.4)	-0.9 ±0.5 (-1.9–0.0)
	5	1.1 ±0.5 (0.4–2.0)	0.5 ±0.5 (-0.3–1.4)	0.1 ±0.5 (-0.7–1.0)	-0.3 ±0.5 (-1.0–0.7)	-0.8 ±0.6 (-1.7–0.2)

[a] The pseudo-CTs were constructed by the introduced dual model HU conversion technique.
[b] 360° VMAT calculated by the XVMC algorithm (MC uncertainty: 0.5%, grid-size: 2 mm).
[c] 7-field IMRT calculated by the AAA (grid-size: 1 mm).

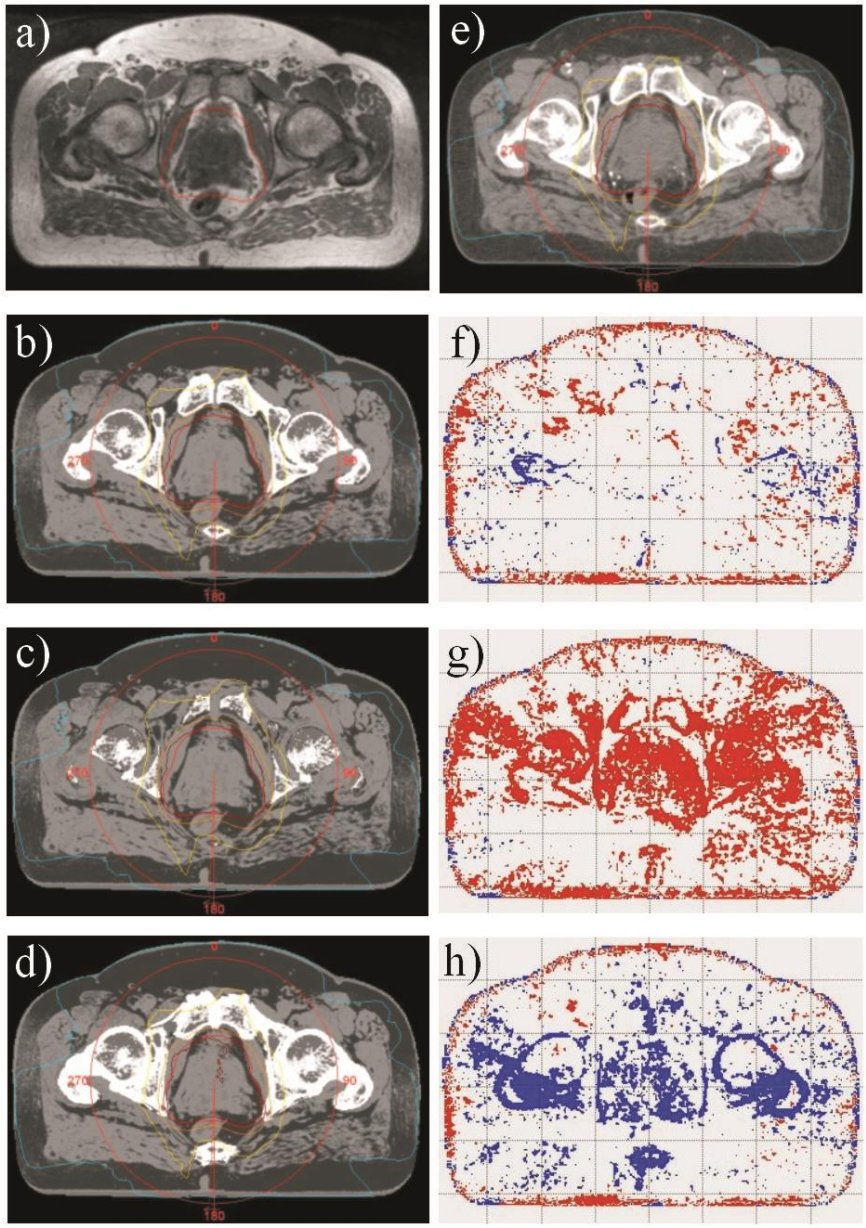

Figure 10. Example patient case presenting dose distribution errors between CT and the heterogeneous pseudo-CTs with the 2D gamma index method for a 360° VMAT plan calculated by the XVMC (MC uncertainty: 0.5%, grid-size: 2 mm). The tested pseudo-CTs are presented as follows; the image obtained by the dual model pseudo-HU conversion technique without additional segmentation error is shown in (b), and the images with additional -3 mm and +3 mm bone segmentation errors are illustrated in (c) and (d), respectively. The reference CT is shown in (e). These planning images illustrate the PTV (red) and the isodose lines for 100% (brown), 90% (orange), 60% (yellow), and 20% (light blue) of prescription dose. Figures from (f) to (h) represent the dose points, which have failed (cold=blue and hot=red) the local gamma index criteria of 1% & 1 mm. The original MR image is shown in (a).

Table 4. Dose distribution comparisons between CTs and the heterogeneous pseudo-CTs[a] with variable-sized bone segments. The percentages of dose points that passed the local 2D Gamma index criteria[b] are shown as mean ±SD (range) for 15 prostate cancer patients.

		Additional systematic error in bone segment				
Plan	Criteria	-2 mm	-1 mm	0 mm	+1 mm	+2 mm
VMAT[c]	1% & 1 mm	82 ±8 (62–94)	88 ±5 (74-96)	88 ±4 (79-96)	86 ±6 (71–94)	79 ±9 (56–90)
	2% & 2 mm	98 ±2 (91–100)	99 ±1 (97–100)	99 ±0 (99–100)	99 ±1 (97–100)	98 ±2 (91–100)
	3% & 3 mm	100 ±1 (98–100)	100 ±0 (all 100)	100 ±0 (all 100)	100 ±0 (all 100)	100 ±0 (99–100)
IMRT[d]	1% & 1 mm	91 ±7 (78–99)	97 ±4 (88-100)	98 ±2 (95-100)	97 ±3 (88–100)	91 ±7 (75–99)
	2% & 2 mm	99 ±1 (95–100)	100 ±0 (99–100)	100 ±0 (all 100)	100 ±0 (all 100)	99 ±2 (94–100)
	3% & 3 mm	100 ±0 (all 100)	100 ±0 (all 100)	100 ±0 (all 100)	100 ±0 (all 100)	100 ±0 (all 100)

[a] The pseudo-CTs were constructed by the introduced dual model HU conversion technique.
[b] The dose evaluations were conducted for a transversal image slice including as many pelvic bones as possible (such as the femoral heads, the greater trochanters, the acetabulums, the pubic bone and the coccyx). Doses < 20% of the maximum were suppressed from the analysis.
[c] 360° VMAT calculated by the XVMC algorithm (MC uncertainty: 0.5%, grid-size: 2 mm).
[d] 7-field IMRT calculated by the AAA (grid-size: 1 mm).

Absorbed doses behind bones

Figure 11 illustrates transversal dose difference profiles (Δ_D by Eq.2) between those behind the bones and those through gelatine only with the single 6 MV radiation field [I]. The measurement results indicated that the dose difference behind the middle part (IC #5) of the femur is smaller (6 MV: 1.3%, 15 MV: 0.9%) compared to the dose difference behind the bone edge (#4), although the distance of radiation traversing through bone is smaller behind the bone edge compared to the middle part. Table 5 presents the statistics of dose deviations between those calculated in pseudo-CTs and those in CT behind the bones [I]. The dose difference profiles in the bulk pseudo-CT was in a different form compared to the profiles obtained in the CT (Figure 11 a). As a result, the dose point deviations rose up to 1.8% behind the middle part of the femur, and up to 2.1% behind the bone edge, but in the opposite direction. The calculated dose difference profiles in the bone conversion pseudo-CT followed more those calculated in the standard CT with maximum dose point deviation of 1.3%. The dose profile shapes behind the femoral head in both pseudo-CTs followed roughly the profile calculated in the CT with maximum deviations of 1.1% and 2.7% in bone conversion- and in bulk pseudo-CTs, respectively. The average deviations of all calculation points behind the bones were also at least a factor two larger in the bulk pseudo-CT than in the bone conversion pseudo-CT (1.1% and 0.4%, respectively, at 6 MV by XVMC). Calculations with the XVMC algorithm indicated that the percentages of all calculation points behind bones with deviation exceeding 1% were 55% (6 MV) and 36% (15 MV) in the bulk pseudo-CT, and 5% (6 MV) and 1% (15 MV) in the bone conversion pseudo-CT. The dose deviations were clearly smaller in the calculations with superposition algorithm than with the XVMC algorithm [I].

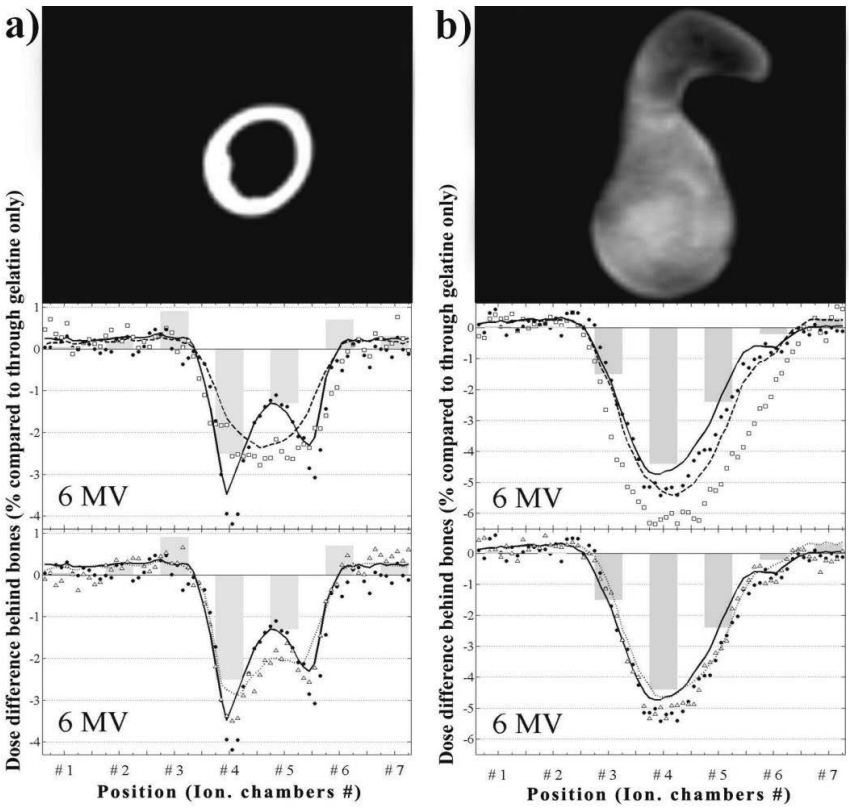

Figure 11. The dose difference profiles (Δ_D by Eq.2) behind bones (radiation traversed through bones) compared to those obtained through gelatine only at 6 MV. a) shows a profile behind a 2.2-cm-thick femur, and b) behind a 5.5-cm-thick femoral head (and greater trochanter). In the diagrams the 5-mm-wide bars represent measurement results and the calculation results in the standard CT image are presented with the solid lines (superposition) and solid dots (XVMC). In the upper diagrams there are presented calculation results in the bulk pseudo-CT with dashed line (superp.) and open squares (XVMC). In the lower diagrams there are illustrated calculation results in the bone conversion pseudo-CT with dashed line (superp.) and open triangles (XVMC).

Table 5. The calculated dose point deviations (absolute values) between those in the bone conversion [and in the bulk] pseudo-CT and those in standard CT of the bone phantom.

Position	Energy (MV)	Calculat. algorithm	Deviation average (%)	Deviation maximum (%)	Correlation coefficient	> 1% dose deviation (%)
Femur (Figure 11 a)	6	Superp.	0.3 [0.6]	0.7 [1.8]	0.91 [0.67]	0 [21]
		XVMC	0.5 [0.8]	1.0 [2.1]	0.88 [0.62]	7 [38]
	15	Superp.	0.2 [0.4]	0.5 [1.1]	0.91 [0.70]	0 [7]
		XVMC	0.4 [0.5]	1.0 [1.3]	0.83 [0.69]	3 [17]
Femoral head (Figure 11 b)	6	Superp.	0.3 [0.6]	0.8 [1.4]	0.97 [0.97]	0 [28]
		XVMC	0.3 [1.4]	0.6 [2.7]	0.99 [0.96]	0 [73]
	15	Superp.	0.2 [0.3]	0.5 [0.9]	0.97 [0.97]	0 [0]
		XVMC	0.2 [0.9]	0.6 [2.0]	0.99 [0.94]	0 [45]

3.4 IGRT with MRI-based reference images

Image guidance with CBCT localization

Table 6 presents the differences in automatic 6D patient position corrections between those obtained by standard reference CT and those achieved either with the heterogeneous pseudo-CT or with the T_1/T_2*-weighted in-phase MR image [IV]. The reported averages and SDs were resulted from recalculations by omitting the major registration outliers (>3 SD, with each registration method ≤10% of registrations). Figure 12 illustrates the differences with 3D automatic grey-value registrations. Figure 13 shows the percentages of registrations passing certain difference criteria with the 6D automatic grey-value registrations. The averages and SDs of registration differences were mostly sub-mms and sub-degrees with the "ClipBox" VOI. With this VOI the maximum differences of all the registrations between CT and heterogeneous pseudo-CT reference images were 2.0 mm (grey-value 3D), 1.7 mm & 1.1° (grey-value 6D), and 1.6 mm & 1.3° (bone 6D), and between CT and MR reference images 4.0 mm (grey-value 3D) and 3.5 mm & 1.6° (grey-value 6D). With the prostate-shaped "Mask" VOI the average registration differences were mainly sub-mms and sub-degrees with SDs ranging up to over 2 mm and 3° (the maximums were >20 mm and >20°). The bony tissue presentation in the MR images was not sufficient for the bone registration (the system reported lack of sufficient tissue and that registrations may be inaccurate). Warnings by the system were detected also with the bulk pseudo-CTs, and thus any of these registration results were not reported.

Table 6. Differences in automatic 6D patient position corrections between those obtained by MRI-based reference images and those achieved with standard reference CTs registered against localization CBCTs as mean ±SD[a].

		CT vs $CBCT_n$ – Pseudo[b] vs $CBCT_n$			CT vs $CBCT_n$ – MRI[c] vs $CBCT_n$		
Registr. method	Dir.	Includ. registr.	Translation (mm)	Rotation (degrees)	Includ. registr.	Translation (mm)	Rotation (degrees)
Grey-value with "ClipBox"	RL	100%	0.3 ±1.0	0.1 ±0.4	92%	0.6 ±1.0	0.0 ±0.5
	IS		0.2 ±0.4	-0.1 ±0.7		-0.6 ±0.6	-0.4 ±0.8
	PA		-0.3 ±0.7	0.0 ±0.4		-1.4 ±0.7	-0.3 ±0.4
Grey-value with "Mask"	RL	92%	0.8 ±1.4	1.1 ±3.3	90%	0.5 ±1.3	1.6 ±3.6
	IS		-0.9 ±1.6	0.1 ±2.4		-0.8 ±1.6	0.3 ±2.6
	PA		-0.4 ±2.2	-0.5 ±2.3		-0.1 ±2.5	0.2 ±2.0
Bone with "ClipBox"	RL	100%	0.3 ±0.9	0.1 ±0.3	-	-	-
	IS		0.1 ±0.4	-0.1 ±0.7		-	-
	PA		-0.3 ±0.7	-0.1 ±0.3		-	-

[a] Recalculated by excluding major registration outliers, i.e. >3 SD.
[b] The heterogeneous pseudo-CT constructed by the dual model HU conversion technique.
[c] The T1/T2*-weighted in-phase MR image series.

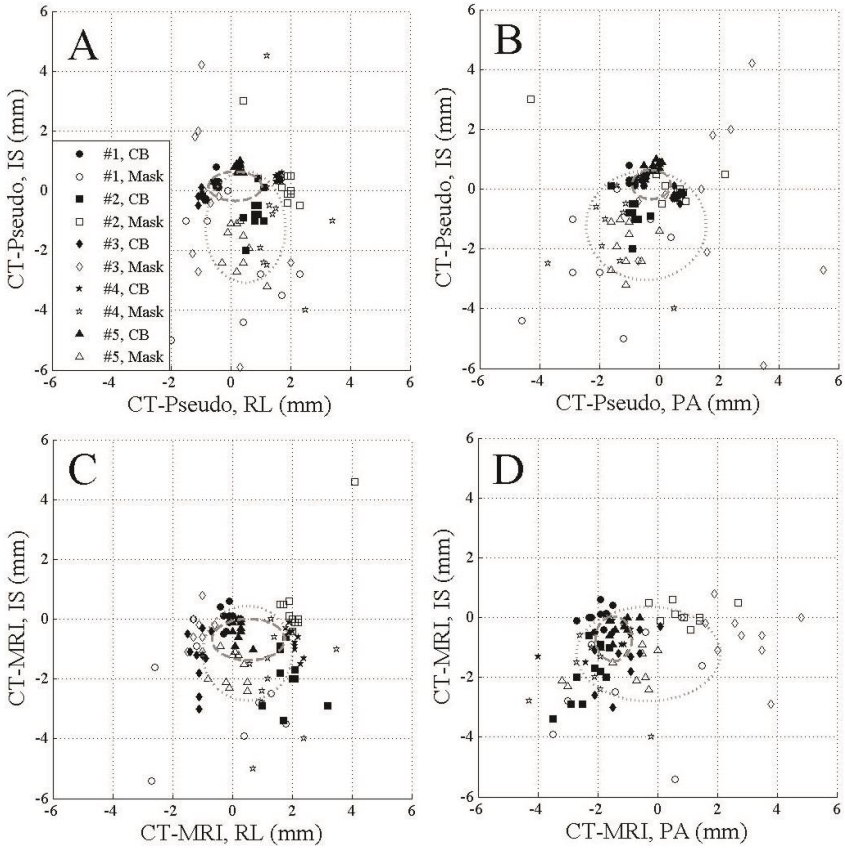

Figure 12. Differences in 3D automatic grey-value registrations between MRI-based and CT reference images i.e. $CTvsCBCT_n$─$MRIvsCBCT_n$ (n=1…50). MRI was the T_1/T_2*-weighted in-phase MR image series and the heterogeneous pseudo-CT was constructed by the dual model pseudo-HU conversion technique. Each symbol represents a patient (from #1 to #5). Solid and open symbols illustrate registrations either with the "ClipBox" VOI or with the "Mask" VOI, respectively. The grey dashed ellipses show SDs (smaller ticks with the "Mask" VOI).

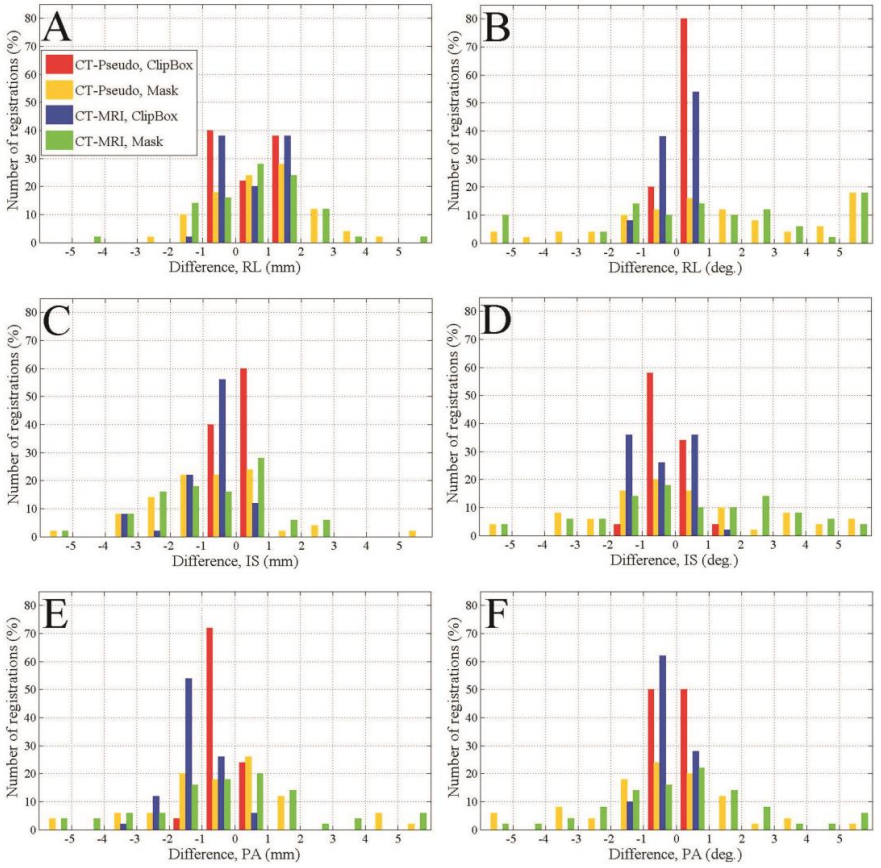

Figure 13. Percentages of differences within certain accuracy criteria (over -5 mm/°, -5<x≤-4 mm/°, -4<x≤-3 mm/°, …, over 5 mm/°) in 6D automatic grey-value registrations between MRI-based and CT reference images i.e. $CTvsCBCT_n$─$MRIvsCBCT_n$ (n=1…50). MRI was the T_1/T_2*-weighted in-phase MR image series and the heterogeneous pseudo-CT was constructed by the dual model pseudo-HU conversion technique.

Image guidance with planar localization

Figure 14 illustrates examples of the reconstructed pseudo-DRRs [IV]. All the applied image similarity metrics were significantly better in agreement between heterogeneous pseudo-DRRs and CT-DRRs than between bulk pseudo-DRRs and CT-DRRs ($p \leq 0.01$) [IV]. Table 7 presents the differences in manual patient position corrections between those obtained by the reference pseudo-DRRs and those achieved with the reference CT-DRRs [IV]. The differences were at their highest in PA direction with means±SDs of -0.3±1.0 & 0.3±1.7 (kV & MV, respectively) between heterogeneous pseudo-DRRs and CT-DRRs, and -0.5±1.4 & -0.3±2.1 between bulk pseudo-DRRs and CT-DRRs.

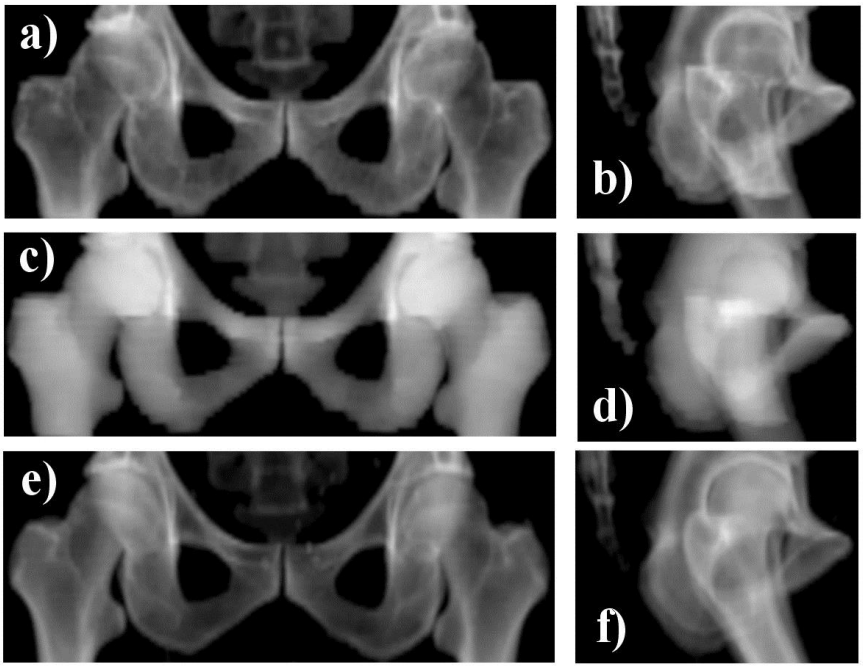

Figure 14. Example reference DRRs reconstructed from different 3D image series: the heterogeneous pseudo-DRRs (a) & (b), the bulk pseudo-DRRs (c) & (d), and the CT-DRRs (e) & (f) (PA & RL, respectively).

Table 7. Differences in manual patient position corrections between those obtained by reference pseudo-DRRs and those achieved with reference CT-DRRs registered against planar localization images as mean ±SD (range).

Planar localiz. images	Transl. direct.	DRR_{CT}[a] vs $planar_n$ – $DRR_{HETER.}$[b] vs $planar_n$ (mm)	DRR_{CT}[a] vs $planar_n$ – DRR_{BULK}[c] vs $planar_n$ (mm)	t- and F-tests (p_t & p_F)
kV	RL	0.1 ±0.5 (-0.8 ─ 1.5)	0.2 ±0.6 (-1.0 ─ 1.4)	0.55 & 0.36
	IS	0.2 ±0.9 (-1.6 ─ 2.8)	0.2 ±1.0 (-1.9 ─ 2.7)	0.72 & 0.14
	PA	-0.3 ±1.0 (-2.5 ─ 1.5)	-0.5 ±1.4 (-3.9 ─ 4.3)	0.33 & 0.01
MV	RL	-0.2 ±0.6 (-1.5 ─ 1.7)	-0.1 ±0.7 (-2.2 ─ 1.2)	0.06 & 0.23
	IS	0.0 ±1.1 (-2.9 ─ 3.0)	0.1 ±1.2 (-3.6 ─ 2.2)	0.25 & 0.40
	PA	0.3 ±1.7 (-5.2 ─ 5.1)	-0.3 ±2.1 (-6.4 ─ 6.1)	0.04 & 0.12

[a] DRR_{CT} was reconstructed from the standard CT image series.
[b] $DRR_{HETER.}$ was reconstructed from the heterogeneous pseudo-CT image series.
[c] DRR_{BULK} was reconstructed from the bulk pseudo-CT image series.

4. Discussion

4.1 Treatment planning with conversion-based heterogeneous pseudo-CT images

The introduced dual model pseudo-HU conversion technique revealed the possibility to construct heterogeneous pseudo-CT images of the pelvis by transforming the intensity values of a single, clinically available MR image into pseudo-HUs [II]. The conversion-based pseudo-CTs enabled the entire RTP workflow of prostate cancer patients by relying merely on MRI as the RT simulator. The dose calculation accuracy in the pseudo-CTs compared to that in standard CTs was within 1%, thus reaching the ultimate RT dose calculation accuracy goal [I-III, 33]. The pseudo-CTs were feasible reference images for both bony tissue -based and soft tissue -based IGRT methods introducing no considerable patient positioning uncertainty compared to the CT-based workflow [IV]. It is important to underline that the MRI-based RTP workflow avoids the additional uncertainty of ~2 mm stemming from the image co-registration necessitated in the RTP process with the target delineation MRI and the planning CT [70, 71].

The pseudo-HU conversion from MRI data is challenging because the MR signal of a particular volume is dependent on the complex relation between multiple parameters e.g. PD, T_1, T_2(*), susceptibility effects and molecular motions (e.g. diffusion and perfusion) [17, 18, 64]. Hence, the conversion of MR image voxel-values is inexplicit and may also depend on imaging platform, parameters, and image processing methods [II]. Although the soft tissue conversion model considered only urine, muscle and fat, also many other soft tissues in the male pelvis, such as the prostate, the seminal vesicles, the penile bulb, the bladder wall, and the bowels were presented in the heterogeneous pseudo-CTs with appropriate HUs [II]. Visual inspection and HU accuracy examinations revealed local uncertainties in tissue representation due to the largest MR signal deviations in each image (caused by e.g. position-related variations in receiver coil sensitivity, and system-related and patient-induced magnetic field inhomogeneities), but more importantly, the model was observed to be robust for normal MR signal level variance and in the absence of visible image artefacts [II]. Considering the model feasibility for clinical use, it is particularly valuable to have one general model functioning sufficiently with all the patients, instead of necessitating patient-specific model adjustment such as MR signal normalization, especially if the adjustments enabled only minor pseudo-HU accuracy improvements, which would have been the case in soft tissues.

The rectal gas and the prostate gold marker HUs were considerably misrepresented in the pseudo-CTs because the soft tissue conversion model transformed low MR signals to the HU of urine. The amount and location of rectal gas is regarded unstable, and thus gas representation with a soft tissue HU in RTP images can be considered appropriate, and can minimize the uncertainties in dose calculation and in the automatic IGRT of the prostate [II, IV, 12, 96]. The gold markers could be presented in the pseudo-CTs by employing a marker-visualizing MRI sequence, and subsequently by inserting marker segments with a representative HU into the pseudo-CT [II, IV, 20]. Nevertheless, the precise soft tissue representation more importantly enabled these images as reference for the state-of-the-art IGRT technique obtaining patient position corrections based on the current position of the soft tissues and the moving organs. Because the pseudo-HU errors in soft tissues were mostly relatively small, further improvements in HU accuracy in the heterogeneous pseudo-CTs should primarily be investigated through refinements on bony tissue conversion.

The conversion model for bones enabled heterogeneous bony tissue representation in the pseudo-CTs [II]. Although HU uncertainty in the pseudo-CTs remained substantially higher compared to the HU deviation levels in CT images, the image information was sufficient for precise and reliable automatic bone registration with the localization CBCTs [II, IV]. The heterogeneous bony tissue representation enabled also reconstruction of pseudo-DRRs with relatively similar contrast with the standard CT-based DRRs resulting in accurate image guidance based on visual inspection of the 2D images [IV]. Although the results illustrated that dose calculation accuracy of 1% can be achieved reliably only by applying the dual model pseudo-HU conversion technique, the heterogeneous bony tissue representation in pseudo-CTs may have had a major impact on dose distribution with the applied IMRT and VMAT treatment plans, due to the applied healthy organ constraints adjusting field directions. For example, by minimizing the absorbed dose to the rectum and the bladder, intensity-modulated techniques tend to deliver the prostate target dose with lateral beam directions, and thus through e.g. greater trochanters, femoral heads and iliac bones. Figure 11 illustrates that the heterogeneous bony tissue representation would be particularly essential in these cases and with one field treatment, such as cranio-spinal, in which the field is directed to the vertebral column including tissues with a wide spectrum of EDs [I, 56]. With treatment techniques employing multiple static fields the influence of high local tissue inhomogeneities on the planned dose may be minimized due to the additional robustness in multi-field treatment plans.

Although the introduced cut-off value for the bone conversion model improved the representation of low-density bony tissues, the wide MR signal range from the bone marrow may still challenge future work aiming to improve tissue representation accuracy [II, 64]. Another major difficulty in bony tissue conversion derives from the minimization of the maximum errors of the few hundred HUs that were detected from the cortical bone. The pseudo-HU errors, however, were mostly randomly distributed to both too high and too low HU representation (Figure 7) [II]. More importantly, the dose distributions investigated particularly behind the different bone parts revealed that the cortical bone pseudo-HU representation enabled achieving dose calculation

accuracy of ~1% (Figure 11) [I]. The cortical bone presentation is challenging due to lack of MR signal with the adopted sequence parameters, and thus the cortical bone image intensity values are combinations of factors such as noise and MR signal bleeding from adjacent tissues (partial volume artefacts and off-resonance effects, e.g. chemical shift) [II]. Further studies could focus on evaluating the model sensitivity to noise level and ultimately aim to introduce methods enabling also accurate bony tissue pseudo-HU conversion requiring no patient-specific adjustments. This would be of particular value considering the model feasibility for routine clinical use. For this purpose, MR sequences with extremely short TEs could prove useful [67-69, 85, 86]. The ultimate goal for the future MRI-based RT research in the pelvis could be generation of heterogeneous pseudo-CTs from MRI data without need for any segmentation. A combination of several images obtained by means of different sequences and/or parameters, such as extremely short TEs, could promote this aim, but would necessitate uncertainty causing image co-registration and most likely the increase in total imaging time [85, 86]. The longer the MR acquisition time, the greater the probability of movement artefacts that can introduce tissue misrepresentation in pseudo-CTs.

As the use of MR images increase in target delineation and in image guidance, the demands for accurate dose calculations in MRI-based RT can be assumed to rise, as well. This can be concluded also by considering the history of CT imaging in RT. In times when the technological improvements in CT scanners and in image processing enabled multi-slice imaging and HU-to-ED calibration, the previously employed homogeneous dose calculation image turned into an image series with heterogeneous ED information, which is today considered the standard image for RT dose calculation [1-5]. With growing interest in developing MRI-based RT methods in clinics, the MRI and RTP system manufacturers are also increasing development and implementation of techniques supporting this workflow [21, 31].

The examinations indicated that the MRI-based dose calculation uncertainty is reduced substantially with the heterogeneous pseudo-CTs compared to conventional pseudo-CTs with homogeneous tissue representations. However, the decision on the complexity of the employed pseudo-CT in MRI-based RT might be also a matter of time and resources that can be spent for the pseudo-CT construction in a clinic, instead of merely considering RTP accuracy. The implemented automatic workflow of the dual model pseudo-HU conversion technique enabled the image transformation from the MR image to the heterogeneous pseudo-CT roughly within 30 seconds [III]. Thus, the precise manual bone outline contouring constitutes the only time-consuming issue limiting the possibilities for employing the technique in a routine clinical workflow. Rapid automatic bone segmentation would be of particular value also when introducing efficient and accurate on-line ART methods in the departments employing MRI-guided RT treatment techniques [22-31]. If the dual model pseudo-HU conversion technique could be applied to the daily localization MR images achieved with appropriate imaging sequence, the on-line ART could be performed with better dose calculation accuracy compared to that reported for CBCT localization images [II, 97-101]. According to Tables 3 and 4, a 2% dose calculation accuracy goal can be

reached with the dual model pseudo-HU conversion technique even if the bone contours were systematically misaligned by 2 mm, and thus still achieving better dose consistency compared to those in bulk pseudo-CTs with precise bone segment [I-III]. Future work aiming to introduce automatic bone contouring for pseudo-CT construction could adopt any of the tested MR sequences for the investigations, because the potential bone outline shift and perturbations did not introduce a restrictive issue with any of the images. However, a major limiting factor in the application of some MR sequences for bone contouring can be the obscure appearance of the cortical bone in the images and the bony tissue definition from these images.

Although this work illustrated major advantages for applying heterogeneous tissue presentation instead of homogeneous simplifications for pseudo-CT construction, the bulk pseudo-CTs can be regarded as an option for RTP in the pelvis, if the assigned bulk pseudo-HUs are appropriately chosen, if the dose calculation uncertainty of 2-3% is clinically permitted, and if the image guidance is conducted based only on the bone outline. Additionally, pseudo-CTs representing large body volumes with average homogeneous pseudo-HUs could be applied to the on-line ART, if conversion techniques cannot be integrated into the MRI-guided RT treatment systems and performed rapidly. Alternatively, it might be optimal to construct the daily pseudo-CTs by deformable co-registration between the on-line MR image and the original heterogeneous pseudo-CT applied to MRI-based RT. The high soft tissue contrast in MR images can be expected to provide valuable information for on-line ART, but if the dose calculation part of the process is inaccurate, the entire gain of MRI-based on-line ART could be questioned.

As the dose calculation uncertainty increases, the room for other error possibilities to reach sufficient overall accuracy level of RTP decreases. The inclusion of the bones into the pseudo-CT even by a simple bulk pseudo-HU assignment minimizes the risk for >3% dose calculation errors [I, III]. The dose evaluations in the bone phantom showed that even less than 2 cm of cortical bone and roughly 5 cm of spongy bone led to 4-5% dose inconsistencies with water-equivalent bone representation [I]. Moreover, with the water-equivalent pseudo-CT the IGRT relying on reference DRRs would be impossible. The image guidance investigations indicated that IGRT with CBCT localization can be conducted with reference MR images, at least with the T_1/T_2*-weighted in-phase images, although the automatic position verification was not as reliable with MR images as with CTs or heterogeneous pseudo-CTs (Table 6, Figures 12 and 13) [IV]. The patient position correction differences between those achieved with the heterogeneous pseudo-CTs compared to those obtained by reference CTs were mainly sub-mms and approximately within the reported uncertainty levels of automatic registration [IV, 12, 13, 93]. Moreover, the automatic registration degrees-of-success (i.e. requiring no further re-adjustments based on visual inspection) were similar to both of these reference images [IV]. The manual patient position verification uncertainty with the heterogeneous pseudo-DRRs was also similar to uncertainty with the CT-based reference images, and thus the reported differences could have resulted from co-registration with either of the DRRs [IV]. According to the observer feedback, the quality of the applied pseudo-DRRs was sufficient for

position verification, and uncertainties mainly stemmed from the localization image quality and FOV [IV]. It is important to underline that these investigations were conducted with pseudo-CTs obtained by employing precisely contoured bone segments. Further studies could aim to determine the needed tissue presentation for reliable IGRT.

Future work could aim quantifying the accuracy of MRI-based RT with the dual model pseudo-HU conversion technique also for pelvic cases other than prostate cancer treatment, and investigate whether the method would prove useful for patients with MRI-compatible hip prosthesis and for brachytherapy treatment planning [16, 102]. Under certain conditions, the conversion technique may work reliably also for other sites on top of pelvis. However, the models should be examined and shown to function appropriately for each site before starting clinical use. If aiming to adopt the presented technique in the presence of air cavities, the technique would most likely need to be substantially modified at least by an additional air cavity contouring and by an assignment of appropriate pseudo-HU conversion also for this segment.

4.2 Uncertainties and limitations in this study

In this work, the uncertainties for the MRI-based RTP were mainly evaluated by regarding the current practise RTP with standard CT as the optimal workflow. The main uncertainties might have derived from factors such as limited voxel-sizes, residual errors from planning CT-to-MR image co-registration, different body positions in the images, movement of tissues, software capabilities of presenting the pixel values, and a limited number of test patients [I-IV, 20, 70, 71, 103, 104]. Potential uncertainty caused by the inherent geometrical distortion in MR images was also included into the evaluations [I-IV, 20]. The sub-mm-sized geometric errors in the vicinity of imaging isocenter cannot introduce relevant uncertainties for the MRI-based RT. However, the system-related distortions increase gradually with distance from the isocenter and could reach relevant magnitudes if a large FOV is needed. In dose calculations, the application of similar body outline contour in both CT and pseudo-CT images for each patient could have minimized the potential uncertainty caused by the geometric errors of body outline. According to Kapanen et al., the body outline shift in the pelvis in the applied MR images is ~1-2 mm on average, and thus the potential body outline shift should not have introduced substantial dose calculation errors with the employed VMAT or multi-field IMRT treatment techniques [II, III, 20]. However, future research could focus on developing appropriate phantom to enable measuring geometric errors precisely within the entire patient FOV (>40 cm). These measurements could aim to determine potential limitations on patient size in MRI-based RT. In these investigations, as in the reported bone outline measurements with ex-vivo bone phantom, it is important to recognize that local susceptibility-induced distortions are unique to individual anatomies and may be different in the complex patient anatomy compared to the phantom. In the present study, changes in tissue characteristics and lack of blood circulation of the adopted ex-vivo specimen may have influenced the MR image intensity values and thus the pseudo-HU

conversion [I, III]. Nevertheless, it is likely that the reported bone outline distortion or the dose profiles would not be substantially different in complex patient anatomy compared to those quantified in this work with the ex-vivo bone phantom [I, III]. It is important to emphasize that the bone outline accuracy was measured only with the images obtained with particular imaging parameters. The susceptibility-related geometrical distortion is dependent on the exact sequence parameters and sampling scheme [21, 54].

The standard CTs were applied to the investigations as they were, and thus rectal gas and effects such as beam hardening, may also have caused uncertainty for the evaluations, in addition to general dose calculation uncertainty in CT images [I-IV]. The currently clinically available dose calculation algorithms and automatic patient position verification software include also their inherent uncertainties [I-IV, 1, 2, 12, 13, 72, 88, 89, 91-96]. Another potential uncertainty-causing issue to the reported dose calculation accuracy in pseudo-CTs may have been induced when optimizing the dose with intensity-modulated techniques in standard CT image and then copying and recalculating the plan in a pseudo-CT. Future work could aim to report the dose calculation accuracy in pseudo-CTs also by optimizing the dose in the image with the simplified tissue representation. In conclusion, it is likely that the actual uncertainty in MRI-based RT dose calculation and image guidance is rather smaller than larger compared to the reported level of MRI-based RT uncertainties.

It is essential to underline that the images used in this work were obtained by the particular equipment and methods [I-IV]. Any changes to MR platform, sequence parameters or pseudo-CT and DRR construction techniques may result in a different outcome. For example, any changes influencing the absolute intensity level in the MR image or its heterogeneity in the image FOV may result in inaccuracies of the pseudo-HU conversion. Changes in sensitivity of the RF coils (local heterogeneities in RF power transmission and intensity of receiver coil), magnetic field inhomogeneities and imaging gradient nonlinearities can increase intensity inhomogeneities, signal loss and local noise. Additionally, the greater the magnetic field gradient (caused by the static magnetic field and tissue magnetization inhomogeneities), the greater the signal loss. Inter-patient variations in the absolute intensity level higher than in the tested images may occur e.g. due to changes in receiver gains or in the body outline distance to the receiver coils. Future work could investigate the potential influence of receiver coil positioning on the quality of conversion-based pseudo-CT images.

Before adopting the dual model pseudo-HU conversion technique in a clinic and after any changes in the MR platform, a verification procedure should be performed to ensure conversion validity in the obtained MR images, even if the MR scanner and the sequence parameters were similar to those applied in this work. Regular QA is also required to verify MR image quality and to detect possible changes in the MR signals to accomplish a reliable MRI-based RTP workflow. Future research could investigate the functioning of the dual model pseudo-HU conversion technique with different equipment. If the method could be used with other MR scanners and imaging parameters, the possibilities for accurate MRI-based RT would increase. Further

studies could also evaluate the feasibility of the technique in obtaining attenuation correction for positron emission tomography/MRI [105].

4.3 Conclusions

This work reached its goals in that it:

1) Developed a dual model pseudo-HU conversion technique to construct heterogeneous pseudo-CT images from MRI data in the pelvis [II].
2) Determined dose calculation accuracy in the obtained pseudo-CTs for prostate cancer patients [I-III].
3) Measured the susceptibility-induced bone outline shift in the employed MR images and quantified the effect of bone outline errors on dose calculation accuracy in the pseudo-CTs [III].
4) Demonstrated that image guidance with X-ray -based localization images can be conducted with MRI-based reference images in the pelvis [IV].
5) Evaluated the benefits of applying heterogeneous pseudo-CTs for MRI-based RT instead of relying on pseudo-CTs with simplified tissue representations [I-IV]
6) Compared the uncertainty level of MRI-based RTP workflow to the standard CT-based process [I-IV]

The presented dual model pseudo-HU conversion technique applies separate conversion models within and outside of bone segment that transform the intensity values of a single clinically available MR image into pseudo-HUs [II]. The obtained images enabled heterogeneous tissue representation with average local uncertainties of ~10 HUs and ~100 HUs in soft- and bony tissues, respectively, compared to those in standard CTs [II]. More importantly, the investigations with sophisticated RTP techniques and dose calculation algorithms illustrated that the ultimate dose calculation accuracy recommendation of 1% can be reached reliably for the target volume and for the healthy tissues by applying the conversion-based heterogeneous pseudo-CTs in MRI-based RTP workflow for prostate cancer patients [I-III]. The examinations with X-ray -based IGRT methods revealed that the heterogeneous pseudo-CTs are feasible reference images for both soft tissue -based and bony tissue -based patient position verification with localization CBCTs, whereas pseudo-DRRs can be employed as reference images for bony tissue -based planar localization. With these reference images, the patient position correction differences compared to those obtained by reference CTs or CT-based DRRs were mainly sub-mms and randomly distributed. The potential susceptibility-induced bone outline shift and geometric perturbations introduced no relevant additional uncertainty for the MRI-based RTP workflow [III]. In conclusion, the results indicate that the accuracy of the introduced MRI-based RTP workflow with the heterogeneous pseudo-CT is approximately within

1% and 1 mm compared to standard CT-based process for prostate cancer patients. Consequently, this work reached its ultimate objective by introducing MRI-based RTP workflow for prostate cancer patients that can be conducted accurately according to required standards of modern RT, thus demonstrating a possibility to omit CT imaging from the process.

References

[1] F. M. Khan; *"The physics of radiation therapy,"* Fourth Edition, Lippincott Williams and Wilkins, Wolters Kluwer business, Philadelphia 2010. ISBN 978-0-7817-8856-4.

[2] A. R. Smith; *"Radiation therapy physics,"* Springer-Verlag, Berlin Heidelberg 1995. ISBN 0-387-55430-0.

[3] R. P. Parker, P. A. Hobday, and K. J. Cassell; *"The direct use of CT numbers in radiotherapy dosage calculations for inhomogeneous media,"* Phys. Med. Biol. 24(4), 802-809 (1979).

[4] U. Schneider, E. Pedroni, and A. Lomax; *"The calibration of CT Hounsfield units for radiotherapy treatment planning,"* Phys. Med. Biol. 41, 111-124 (1996).

[5] S. J. Thomas, *"Relative electron density calibration of CT scanners for radiotherapy treatment planning,"* Br. J. Radiol. 72, 781-786 (1999).

[6] European Commission, *Criteria for acceptability of medical radiological equipment used in diagnostic radiology, nuclear medicine and radiotherapy,* Report 162, http://ec.europa.eu/energy/nuclear/radiation_protection/doc/publication/162.pdf,63-69 (2012).

[7] S. Kuttner, R. Bujila, M. Kortesniemi, H. Andersson, L. Kull, B. H. Österås, J. Thygesen, and I. S. Tarp; *"A proposed protocol for acceptance and constancy control of computed tomography systems: A Nordic Association for Clinical Physics (NACP) work group report,"* Acta Radiol. 1-11 (2012).

[8] B. Fraass, K. Doppke, M. Hunt, G. Kutcher, G. Starkschall, R. Stern, and J. Van Dyke; *"American Association of Physicists in Medicine Radiation Therapy Committee Task Group 53: Quality assurance for clinical radiotherapy treatment planning,"* Med. Phys. 25(10), 1773-1829 (1998).

[9] M. A. Ebert, J. Lambert, and P. B. Greer; *"CT-ED conversion on a GE Lightspeed-RT scanner: influence of scanner settings,"* Australasian Phys. & Eng. Sc. Med. 31(2), 154-159 (2008).

[10] W. Skrzynski, S. Zielinska-Dabrowska, M. Wachowicz, W. Slusarczyk-Kacprzyk, P. F. Kukolowicz, and W. Bulski; *"Computed tomography as a source of electron density information for radiation treatment planning,"* Strahlent. Onkol. 6, 327-332 (2010).

[11] D. A. Jaffray, J. H. Siewerdsen, J. W. Wong, and A. A. Martinez; *"Flat-panel cone-beam computed tomography for image-guided radiation therapy,"* Int. J. Radiat. Oncol. Biol. Phys. 53(5), 1337-1349 (2002).

[12] M. H. P. Smitsmans, J. W. H. Wolthaus, X. Artignan, J. de Bois, D. A. Jaffray, J. V. Lebesque, and M. van Herk; *"Automatic localization of the prostate for on-line or off-line image-guided radiotherapy,"* Int. J. Radiat. Oncol. Biol. Phys. 60(2), 623-635 (2004).

[13] M. H. P. Smitsmans, J. de Bois, J.-J. Sonke, A. Betgen, L- J. Zijp, D. A. Jaffray, J. V. Lebesque, and M. van Herk; *"Automatic prostate localization on cone-beam CT scans for high precision image-guided radiotherapy,"* Int. J. Radiat. Oncol. Biol. Phys. 63(4), 975-984 (2005).

[14] V. Khoo and D. Joon; *"New developments in MRI for target volume delineation in radiotherapy,"* Br. J. Radiol. 79, 2-15 (2006).

[15] A. Sciarra, J. Barentsz, A. Bjartell, J. Eastham, H. Hricak, V. Panebianco, and J. A. Witjes; *"Advances in magnetic resonance imaging: How they are changing the management of prostate cancer,"* Eur. Urol. 59, 962-977 (2011).

[16] P. Dirix, K. Haustermans, and V. Vandecaveye; *"The value of Magnetic resonance imaging for radiotherapy planning,"* Semin. Radiat. Oncol. 24, 151-159 (2014).

[17] D. W. McRobbie, E. A. Moore, M. J. Graves, and M. R. Prince; *"MRI from picture to proton,"* Second edition, University press, Cambridge 2010. ISBN 978-0-521-68384-5.

[18] Z. Liang, and P. C. Lauterbur; *"Principles of magnetic resonance imaging,"* IEEE press, The institute of electrical and electronics engineers Inc., New York 2000. ISBN 0-7803-4723-4.

[19] M. Seitz, A. Shukla-Dave, A, Bjartell, K. Touijer, A. Sciarra, P. J. Bastian, C. Stief, H. Hricak, and A. Graser; *"Functional magnetic resonance imaging in prostate cancer,"* Eur. Urol. 55, 801-814 (2009).

[20] M. Kapanen, J. Collan, A. Beule, T. Seppälä, K. Saarilahti, and M. Tenhunen; *"Commissioning of MRI-only based treatment planning procedure for external beam radiotherapy of prostate,"* Magn. Reson. Med. 70, 127-135 (2013).

[21] G. P. Liney, and M. A. Moerland; *"Magnetic resonance imaging acquisition techniques for radiotherapy planning,"* Semin. Radiat. Oncol. 24, 160-168 (2014).

[22] T. Stanescu, T. Tadic, and D. A. Jaffray; *"Commissioning of an MR-guided radiation therapy system,"* Radiat. Oncol. Biol. Phys. 90(1), 94-95 (2014).

[23] D. A. Jaffray, M. C. Carlone, M. F. Milosevic, S. L. Breen, T. Stanescu, A. Rink, H. Alasti, A. Simeonov, M. C. Sweitzer, and J. D. Winter; *"A facility for magnetic resonance-guided radiation therapy,"* Semin. Radiat. Oncol. 24, 193-195 (2014).

[24] M. Karlsson, M. G. Karlsson, T. Nyholm, C. Amies, and B. Zackrisson; *"Dedicated magnetic resonance imaging in the radiotherapy clinic,"* Radiat. Oncol. Biol. Phys. 74, 644-651 (2009).

[25] B. G. Fallone, B. Murray, S. Rathee, T. Stanescu, S. Steciw, S. Vidakovic, E. Blosser, and D. Tymofichuk; *"First MR images obtained during megavoltage photon irradiation from a prototype integrated linac-MR system,"* Med. Phys. 36(6), 2084-2088 (2009).

[26] B. Raaymakers, J. Lagendijk, J. Overweg, J. Kok, A. Raaijmakers, E. Kerkhof, R. van der Put, I. Meijsing, S. Crijns, F. Benedosso, M. van Vulpen, C. Graaff, J. Allen, and K. Brown; *"Integrating a 1.5 T MRI scanner with a 6 MV accelerator: proof of concept,"* Phys. Med. Biol. 54, 229-237 (2009).

[27] E. Kerkhof, J. Balter, K. Vineberg and B. Raaymakers; *"Treatment plan adaptation for MRI-guided radiotherapy using solely MRI data: a CT-based simulation study,"* Phys. Med. Biol. 55, 433-440 (2010).

[28] P. J. Keall, M. Barton, and S. Crozier, *"The Australian magnetic resonance imaging-Linac program,"* Semin. Radiat. Oncol. 24, 203-206 (2014).

[29] T. Kron, D. Eyles, S. L. John, and J. Battista; *"Magnetic resonance imaging for adaptive cobalt tomotherapy: A proposal,"* J. Med. Phys. 31(4), 242-254 (2006).

[30] O. Green, S. Goddu, and S. Mutic; *"Commissioning and quality assurance of the first commercial hybrid MRI-IMRT system,"* Med. Phys. 39(6), 3785 (2012).

[31] J. J. W. Lagendijk, B. W. Raaymakers, C. A. T. Van den Berg, M. A. Moerland, M. E. Philippens, and M. van Vulpen; *"MR guidance in radiotherapy,"* Phys. Med. Biol. 59, R349-R369 (2014).

[32] International Commission on Radiation Units and Measurements (ICRU); *"Use of computers in external beam radiotherapy procedures with high-energy photons and electrons,"* ICRU Report 42, http://jicru.oxfordjournals.org, 49-50 (1987).

[33] A. Ahnesjö and M. M. Aspradakis; *"Dose calculations for external photon beams in radiotherapy,"* Phys. Med. Biol. 44, R99-R155 (1999).

[34] European Commission; *"Criteria for acceptability of medical radiological equipment used in diagnostic radiology, nuclear medicine and radiotherapy,"* Report 162, http://ec.europa.eu/energy/nuclear/radiation_protection/doc/publication/162.pdf, 63-69 (2012).

[35] Y Lee, M. Bollet, G. Charles-Edwards, M. Flower, M. Leach, H. McNair, E. Moore, C. Rowbottom, and S. Webb; *"Radiotherapy treatment planning of prostate cancer using magnetic resonance imaging alone,"* Radiother. Oncol. 66, 203-216 (2003).

[36] L. Chen, R. A. Price Jr, T.-B. Nguyen, L. Wang, J. S. Li, L. Qin, M. Ding, E. Palacio, C.-M. Ma, and A. Pollack; *"Dosimetric evaluation of MRI-based treatment planning for prostate cancer,"* Phys. Med. Biol. 49, 5157-5170 (2004).

[37] D. Pasqueir, N. Betrouni, M. Vermandel, T. Lacornerie, T. Lartigau, and J. Rousseau; *"MRI alone simulation for conformal radiation therapy of prostate cancer: technical aspects,"* Conf. Proc. IEEE Eng. Med. Biol. Soc. 1, 160-163 (2006).

[38] T. Stanescu, J. Hans-Sonke, P. Stavrev, and B. G. Fallone; *"3T MR-based treatment planning for radiotherapy of brain lesions,"* Radiol. Oncol. 40(2), 125-132 (2006).

[39] R. Prabhakar, P. Julka, T. Ganesh, A. Munshi, R. Joshi and G. Rath; *"Feasability of using MRI alone for 3D radiation treatment planning in brain tumors,"* Jpn. J. Clin. Oncol. 37(6), 405-411 (2007).

[40] D. Mah, M. Steckner, A. Hanlon, G. Freeman, B. Milestone, R. Mitra, H. Shukla, B. Movsas, E. Horwitz, P. P. Väisänen, and G. E. Hanks; *"MRI simulation: effect of gradient distortions on three-dimensional prostate cancer plans,"* Int. J. Radiat. Oncol. Biol. Phys. 53(3), 757-765 (2002).

[41] D. Mah, M. Steckner, E. Palacio, R. Mitra, T. Richardson, and G. E. Hanks; *"Characteristics and quality assurance of a dedicated open 0.23 T MRI for radiation therapy simulation,"* Med. Phys. 29(11), 2541-2547 (2002).

[42] L. Chen, R. A. Price, L. Wang, J. Li, L. Qin, S. McNeeley, C-M C. Ma, G. M. Freedman, and A. Pollack; *"MRI-based treatment planning for radiotherapy: dosimetric verification for prostate IMRT,"* Int. J. Radiat. Oncol. Biol. Phys. 60(2), 636-647 (2004).

[43] B. Petersch, J. Bogner, A. Fransson, T. Lorang, and R. Pötter, *"Effects of geometric distortion in 0.2 T MRI on radiotherapy treatment planning of prostate cancer,"* Radiother. Oncol. 71, 55-64 (2004).

[44] Z. Chen, C-M Ma, K. Paskalev, J. Li, J. Yang, T. Richardson, L. Palacio, X. Xu, and L. Chen; *"Investigation of MR image distortion for radiotherapy treatment planning of prostate cancer,"* Phys. Med. Biol. 51, 1393-1403 (2006).

[45] S. P. M. Crijns, C. J. G. Bakker, P. R. Seebinck, H. de Leeuw, J. J. W. Lagendijk, and B. W. Raaymakers; *"Towards inherently distortion-free MR images for image-guided radiotherapy on an MRI accelerator,"* Phys. Med. Biol. 57, 1349-1358 (2012).

[46] T. Stanescu, H.-S. Jans, N. Pervez, P. Stavrev, and B. G. Fallone; *"A study on the magnetic resonance imaging (MRI)-based radiation treatment planning of intracranial lesions,"* Phys. Med. Biol. 53, 3579-3593 (2008).

[47] D. Wang, W. Strugnell, G. Cowin, D. M. Doddrell, and R. Slaughter; *"Geometric distortion in clinical MRI systems; Part I: evaluation using a 3D phantom,"* Magn. Reson. Imaging 22, 1211-1221 (2004).

[48] D. Wang, W. Strugnell, G. Cowin, D. M. Doddrell, and R. Slaughter; *"Geometric distortion in clinical MRI systems; Part II: correction using a 3D phantom,"* Magn. Reson. Imaging 22, 1223-1232 (2004).

[49] L. N. Baldwin, K. Wachowicz, and B. G. Fallone; *"A two-step scheme for distortion rectification of magnetic resonance images,"* Med. Phys. 36(9), 3917-3926 (2009).

[50] A. Fransson, P. Andreo, and R. Pötter; *"Aspects of image distortions in radiotherapy treatment planning,"* Strahlenther. Oncol. 177, 59-73 (2001).

[51] D. Pasqueir D, and E. Lartigau; *"MRI prostate radiation therapy planning: when the patient distorts his own image,"* Radiother. Oncol. 102, 161-163 (2012).

[52] K. Ludeke, P. Roschmann, and R. Tischler, *"Susceptibility artefacts in NMR imaging;"* Magn. Reson. Imaging 3, 329-343 (1985).

[53] J. F. Schenck; *"The role of magnetic susceptibility in magnetic resonance imaging: MRI magnetic compatibility of the first and second kinds,"* Med. Phys. 23, 815-850 (1996).

[54] T. Stanescu, K. Wachowicz, and D. A. Jaffray; *"Characterization of tissue magnetic susceptibility-induced distortions for MRIgRT,"* Med. Phys. 39, 7185-7193 (2012).

[55] J. Hopkins, and F. Wehrli; *"Magnetic susceptibility measurement of insoluble solids by NMR: magnetic susceptibility of bone,"* Magn. Reson. Med. 37, 494-500 (1997).

[56] H. Q. Woodard and D. R. White; *"The composition of body tissues,"* Br. J. Radiol. 59, 1209-1219 (1986).

[57] D. R. White, H. Q. Woodard, and S. M. Hammond; *"Average soft-tissue and bone models for use in radiation dosimetry,"* Br. J. Radiol. 60, 907-913 (1987).

[58] International Commission on Radiation Units and Measurements (ICRU); *"Photon, electron, proton and neutron interaction data for body tissues,"* ICRU Report 46, http://jicru.oxfordjournals.org, Appendix A, 11-12 (1992).

[59] K. Eilertsen, L. Vestad, O. Geier, A. Skretting; *"A simulation of MRI based dose calculations on the basis of radiotherapy planning CT images,"* Acta Oncol. 47, 1294-1302 (2008).

[60] J. Jonsson, M. G. Karlsson, M. Karlsson, and T. Nyholm; *"Treatment planning using MRI data: an analysis of the dose calculation accuracy for different treatment regions,"* Radiat. Oncol. 5, 62 (2010).

[61] J. Lambert, P. Greer, F. Menk, J. Patterson, J. Parker, K. Dahl, S. Gupta, A. Capp, C. Wratten, C. Tang, M. Kumar, J. Dowling, S. Hauville, C. Hughes, K. Fisher, P. Lau, J. Denham, and O. Salvado; *"MRI-guided prostate radiation therapy planning: Investigation of dosimetric accuracy of MRI-based dose planning,"* Radiother. Oncol. 98, 330-334 (2010).

[62] P. B. Greer, J. A. Dowling, J. A. Lambert, J. Fripp, J. Parker, J. W. Denham, C. Wratten, A. Capp, and O. Salvado; *"A magnetic resonance imaging-based workflow for planning radiation therapy for prostate cancer,"* MJA 194(4), 24-27 (2011).

[63] J. Dowling, J. Lambert, J Parker, O. Salvado, J. Fripp, A. Capp, C. Wratten, J. Denham, P. Greer; *"An atlas-based electron density mapping method for magnetic resonance imaging (MRI)-alone treatment planning and adaptive MRI-based prostate radiation therapy,"* Int. Radiat. Oncol. Biol. Phys. 83, 5-11 (2012).

[64] M. Kapanen, and M. Tenhunen; *"T1/T2*-weighted MRI provides clinically relevant pseudo-CT density data from pelvic bones in MRI-only based radiotherapy treatment planning."* Acta Oncol. 52(3), 612-618 (2013).

[65] H. Yu, C. Caldwell, J. Balogh, and K. Mah; *"Toward magnetic resonance-only simulation: segmentation of bone in MR for radiation therapy verification of the head,"* Int. J. Radiat. Oncol. Biol. Phys. 89(3), 649-657 (2014).

[66] A. Karotki, K. Mah, G. Meijer and M. Meltsner, *"Comparison of bulk electron density and voxel-based electron density treatment planning,"* J. appl. Clin. Med. Phys. 12(4), 97-104 (2011).

[67] A. Johansson, M. Karlsson, and T. Nyholm; *"CT substitute derived from MRI sequences with ultrashort echo time,"* Med. Phys. 38(5), 2708-2714 (2011).

[68] A. Johansson, M. Karlsson, J. Yu, T. Asklund, and T. Nyholm; *"Voxel-wise uncertainty in CT substitute derived from MRI,"* Med. Phys. 39(6), 3283-3290 (2012).

[69] A. Johansson, A. Garpebring, M. Karlsson, T. Asklund, and T. Nyholm; *"Improved quality of computed tomography substitute derived from magnetic resonance (MR) data by incorporation of spatial information – potential application for MR-only radiotherapy and attenuation correction in positron emission tomography,"* Acta Oncol. 52, 1369-73 (2013).

[70] T. Nyholm, and J. Jonsson; *"Counterpoint: opportunities and challenges of a magnetic resonance imaging-only radiotherapy work flow,"* Semin. Radiat. Oncol. 24, 175-180 (2014).

[71] T. Nyholm, M. Nyberg, M. G. Karlsson, and M. Karlsson; *"Systematisation of spatial uncertainties for com-parison between a MR and CT-based radiotherapy workflow for prostate treatments,"* Radiat. Oncol. 4, 54 (2009).

[72] M. Fippel; *"Fast Monte Carlo dose calculation for photon beams based on the VMC electron algorithm,"* Med. Phys. 26(8), 1466-1475 (1999).

[73] C. R. Ramsey and A. L. Oliver; *"Magnetic resonance imaging based digitally reconstructed radiographs, virtual simulation, and three-dimensional treatment planning for brain neoplasms,"* Med. Phys. 25,1928-1934 (1998).

[74] L. Chen, T. B. Nguyen, É Jones, Z. Chen, W. Luo, L. Wang, R. A. Price, A. Pollack and C. Ma; *"Magnetic resonance-based treatment planning for prostate intensity-modulated radiotherapy: creation of digitally reconstructed radiographs,"* Int. J. Radiat. Oncol. Biol. Phys. 68, 903-911 (2007).

[75] W. T. Dixon; *"Simple proton spectroscopic imaging,"* Radiology 153, 189-194 (1984).

[76] J. Ma; *"Breath-hold water and fat imaging using a dual-echo two-point Dixon technique with an efficient and robust phase-correction algorithm,"* Magn. Reson. Med. 52, 415-419 (2004).

[77] A. Janke, H. Zhao, G. J. Cowin, G. J. Galloway, and D. M. Doddrell; *"Use of spherical harmonic deconvolution methods to compensate for nonlinear gradient effects on MRI images,"* Magn. Reson. Med. 52, 115-122 (2004).

[78] S. J. Doran, L. Charles-Edwards, S. A. Reinsberg, and M. O. Leach; *"A complete distortion correction for MR images: I. Gradient warp correction,"* Phys. Med. Biol. 50, 1343-1361 (2005).

[79] R. C. Grimm, D. G. Kruger, J. A. Polzin, and S. J. Riederer; *"Sub-second 3D image reconstruction with Gradwarp correction in moving table MRI,"* Proc. Intl. Soc. Mag. Reson. Med. 14, 2367 (2006).

[80] U. Vovk, F. Pernus, and B. Likar; *"A review of methods for correction of intensity inhomogeneity in MRI,"* IEEE Trans. Med. Imag. 26(3), 405-421 (2007).

[81] S. Majundar, H. K. Genant, S. Grampp, D. C. Newitt, V. H. Truong, J. C. Lin, and A. Mathur; *"Correlation of trabecular bone structure with age, bone mineral density, and osteoporotic status: in vivo studies in the distal radius using high resolution magnetic resonance imaging,"* J. Bone Miner. Res. 12, 111-118 (1997).

[82] S. Majundar, D. Thomasson, A. Shimakawa, and H. K. Genant; *"Quantitation of the susceptibility difference between trabecular bone and bone marrow: experimental studies,"* Magn. Reson. Med. 22, 111-127 (1991).

[83] J. C. Ford, F. W. Wehrli, and H. Chung; *"Magnetic field distribution in models of trabecular bone,"* Magn. Reson. Med. 30, 373-379 (1993).

[84] T. M. Link, S. Majumdar, P. Augat, J. C. Lin, D. Newitt, N. E. Lane, and H. K. Genant; *"Proximal femur: assessment for osteoporosis with T2* decay charasteristics at MR imaging,"* Radiology 209, 531-536 (1998).

[85] J. Du and G. M. Bydder; *"Qualitative and quantitative ultrashort-TE MRI of cortical bone,"* NMR Biomed. 26, 489-506 (2013).

[86] M. Weiger, D. O. Brunner, B. E. Dietrich, C. F. Müller, and K. P. Pruessmann; *"ZTE imaging in humans,"* Magn. Reson. Med. 70, 328-332 (2013).

[87] B. C. vande Berg, J. Malghem, F. E. Lecouvet, and B. Maldague; *"Magnetic resonance imaging of the normal bone marrow,"* Skeletal Radiol. 27(9), 471-483 (1998).

[88] A. van Esch, L. Tillikainen, J. Pyykkönen, M. Tenhunen, H. Helminen, S. Siljamäki, J. Alakuijala, M. Paiusco, M. Iori, and D. P. Huyskens; *"Testing of the analytical anisotropic algorithm for photon dose calculation,"* Med. Phys. 33(41), 30-48 (2006).

[89] D. Robinson; *"Inhomogeneity correction and the analytic anisotropic algorithm,"* J. Appl. Clin. Med. Phys. 9(2), 112-122 (2008).

[90] D. Low, W. Harms, S. Mutic, and J. Purdy; *"A technique for the quantitative evaluation of dose distributions,"* Med. Phys. 25(5), 656-661 (1998).

[91] J. Korhonen; *"Using volumetric-modulated arc therapy and cone-beam computed tomography image guidance with six degrees of freedom in patient positioning for the radiation therapy of patients with bladder cancer,"* Aalto University, School of Electrical engineering, Health Technology, Helsinki, Finland, Master's Thesis, http://urn.fi/URN:NBN:fi:aalto-201207022699 (2011).

[92] L. Tuomikoski, J. Korhonen, J. Collan, J. Keyriläinen, H. Visapää, J. Sairanen, K. Saarilahti, and M. Tenhunen; *"Implementation of adaptive radiation therapy for urinary bladder caricinoma: Imaging, planning and image guidance,"* Acta Oncol. 52, 1451-1457 (2013).

[93] D. Létourneau, A. A. Martinez, D. Lockman, D. Yan, C. Vargas, G. Ivaldi, and J. Wong; *"Assessment of residual error for online cone-beam CT-guided treatment of prostate cancer patients,"* Int. J. Radiat. Oncol. Biol. Phys. 62, 1239-1246 (2005).

[94] J. R. Sykes, D. S. Brettle, D. R. Magee, and D. I. Thwaites; *"Investigation of uncertainties in image registration of cone-beam CT to CT on an image-guided radiotherapy system,"* Phys. Med. Biol. 54, 7263-7283 (2009).

[95] M. van Herk and H. M. Kooy; *"Automatic three-dimensional correlation of CT-CT, CT-MRI, and CT-SPECT using chamfer matching,"* Med. Phys. 21, 1163-1178 (1994).

[96] M. H. P. Smitsmans, F. J. Pos, J. de Bois, W. D. Heemsbergen, J.-J. Sonke, J. V. Lebesque, and M. van Herk; *"The influence of dietary protocol on cone beam CT-guided radiotherapy for prostate cancer patients,"* Int. J. Radiat. Oncol. Biol. Phys. 71(4), 1279-1286 (2008).

[97] A. Richter, Q. Hu, D. Steglich, K. Baier, J. Wilbert, M. Guckenberger, and M. Flentje; *"Investigation of the usability of conebeam CT data sets for dose calculation,"* Rad. Oncol. 3(42), 1-13 (2008).

[98] R. Varadhan, S. K. Hui, S. Way, and K. Nisi; *"Assessing prostate, bladder and rectal doses during image guided radiation therapy – need for plan adaptation?"* J. Appl. Clin. Med. Phys. 10(3), 56-74 (2009).

[99] H. Guan and H. Dong; *"Dose calculation accuracy using cone-beam CT (CBCT) for pelvic adaptive radiotherapy,"* Phys. Med. Biol. 54, 6239-6250 (2009).

[100] I. Fotina, J. Hopfgartner, M. Stock, T. Steininger, C. Lütgendorf-Caucig, and D. Georg; *"Feasibility of CBCT-based dose calculation: Comparative analysis of HU adjustment techniques,"* Radiother. Oncol. 104, 249-256 (2012).

[101] J. Cheung, J.-F. Aubry, S. S. Yom, A. R. Gottschalk, J. C. Cell, and J. Pouliot; *"Dose recalculation and the dose-guided radiation therapy (DGRT) process using megavoltage cone-beam CT,"* Int. J. Radiat. Oncol. Biol. Phys. 74(2), 583-592 (2009).

[102] K. Tanderup, A. N. Viswanathan, C. Kirisits, and S. J. Frank; *"Magnetic resonance image guided brachytherapy,"* Semin. Radiat. Oncol. 24, 181-191 (2014).

[103] M. J. Zelefsky, D. Crean, G. S. Mageras, O. Lyass, L. Happersett, C. C. Ling, S. A. Leibel, Z. Fuks, S. Bull, H. M. Kooy, M. van Herk, and G. J. Kutcher; *"Quantification and predictors of prostate position variability in 50 patients evaluated with multiple CT scans during conformal radiotherapy,"* Radiother. Oncol. 50, 225-234 (1999).

[104] A. N. T. J. Kotte, P. Hofman, J. J. W. Lagendijk, M. van Pulpen, and U. A. van der Heide; *"Intrafraction motion of the prostate during external-beam radiation therapy: analysis of 427 patients with implanted fiducial markers,"* Int. J. Radiat. Oncol. Biol. Phys. 63, 975-984 (2005).

[105] I. Bezrukov, F. Mantlik, H. Schmidt, B. Schölkopf, and B. J. Pichler; *"MR-based PET attenuation correction for PET/MR imaging,"* Semin. Nucl. Med. 43, 45-59 (2013).

Magnetic resonance imaging (MRI) is increasingly applied for external radiation therapy (RT) target delineation owing to the superior soft tissue contrast in MR images compared to that in computed tomography (CT) images. CT image has remained the standard reference for other parts of RT treatment planning (RTP) workflow; dose calculation and image guidance, due to the restrictive features of MR images for these tasks; such as lack of explicit relation between MR signals and electron densities. Consequently, currently widely employed practice of RTP workflow necessitates imaging with two modalities that increases RTP uncertainty by requisite image co-registration, exposes patients' healthy tissues to the additional ionizing radiation applied in CT, and increases hospital staff workload. This study introduces RTP workflow for prostate cancer patients that relies solely on MRI-based RTP images, and shows that this process can be conducted accurately according to required standards of modern RT, thus demonstrating a possibility to omit CT imaging from the workflow.

Aalto-DD 35/2015

ISBN 978-952-60-6123-8 (printed)
ISBN 978-952-60-6124-5 (pdf)
ISSN-L 1799-4934
ISSN 1799-4934 (printed)
ISSN 1799-4942 (pdf)

Aalto University
School of Electrical Engineering
Aalto University School of Electrical Engineering
www.aalto.fi

BUSINESS + ECONOMY

ART + DESIGN + ARCHITECTURE

SCIENCE + TECHNOLOGY

CROSSOVER

DOCTORAL DISSERTATIONS